Title: Magnetic soft micro-fiberbots for robotic embolization

Authors:

Xurui Liu[1,2]†, Liu Wang[3]†, Yuanzhuo Xiang[2]†, Fan Liao[1,2], Na Li[1, 2], Jiyu Li[3], Jiaxin Wang[4] Qingyang Wu[1, 2], Cheng Zhou[1, 2], Youzhou Yang[1, 2], Yuanshi Kou[1, 2], Yueying Yang[1, 2], Hanchuan Tang[1, 2], Ning Zhou[5], Chidan Wan[6], Guang-Zhong Yang[7]*, Guangming Tao[2, 8]*, Jianfeng Zang[1, 2, 9]*

Affiliations:

[1]School of Integrated Circuits, Huazhong University of Science and Technology, Wuhan 430074, China

[2]Wuhan National Laboratory for Optoelectronics, Huazhong University of Science and Technology, Wuhan 430074, China

[3]CAS Key Laboratory of Mechanical Behavior and Design of Materials, Department of Modern Mechanics, University of Science and Technology of China, Hefei 230026, PR China

[4]Department of Urology, Tongji Hospital, Tongji Medical College, Huazhong University of Science and Technology, Wuhan 430030, PR China.

[5]Division of Cardiology, Department of Internal Medicine, Tongji Hospital of Tongji Medical College of Huazhong University of Science and Technology, Wuhan 430074, China

[6]Department of Hepatobiliary Surgery, Union Hospital, Tongji Medical College, Huazhong University of Science and Technology, Wuhan 430074, China

[7]Institute of Medical Robotics, Shanghai Jiao Tong University, Shanghai 200240, China

[8]The State Key Laboratory of Material Processing and Die & Mould Technology, School of Materials Science and Engineering, Huazhong University of Science and Technology, Wuhan, 430074 China

[9]The State Key Laboratory of Digital Manufacturing Equipment and Technology, Huazhong University of Science and Technology, Wuhan 430074, China

†These authors contributed equally to this work.

*Corresponding authors. Email: gzyang@sjtu.edu.cn (G.-Z.Y.); tao@hust.edu.cn (G.T.); jfzang@hust.edu.cn (J.Z.)

Abstract: Cerebral aneurysms and brain tumors are leading life-threatening diseases worldwide. By deliberately occluding the target lesion to reduce the blood supply, embolization has been widely used clinically to treat cerebral aneurysms and brain tumors. Conventional embolization is usually performed by threading a catheter through blood vessels to the target lesion, which is often limited by the poor steerability of the catheter in complex neurovascular networks, especially in submillimeter regions. Here we propose magnetic soft micro-fiberbots with high steerability, reliable maneuverability, and multi-modal shape reconfigurability to perform robotic embolization in submillimeter regions via a remote, untethered, and magnetically controllable manner. Magnetic soft micro-fiberbots are fabricated by thermal drawing magnetic soft composite (i.e., hard-magnetic particles dispersed in thermoplastic matrices) into micro-fibers, followed by magnetizing and molding procedures to endow a helical magnetic polarity. By controlling magnetic fields, magnetic soft micro-fiberbots exhibit reversible elongated/aggregated shape-morphing and helical propulsion in flow conditions, allowing for controllable navigation through complex vasculature and robotic embolization in submillimeter regions. We performed 1) in vitro embolization of aneurysm and tumor in neurovascular phantoms and 2) in vivo embolization of a rabbit femoral artery model under real-time fluoroscopy. They demonstrate the

potential clinical value of our work, paving the way for a new embolization scheme in robotic settings.

One-Sentence Summary: We present magnetic soft micro-fiberbots that can perform robotic embolization in blood vessels in vivo in a remote, untethered, and magnetically controllable manner.

Main Text:

INTRODUCTION

Cerebral aneurysms and brain tumors are leading causes of mortality, killing more than 750,000 people annually worldwide *(1-2)*. Before an open surgery is administered, embolization recently has become a prevailing minimally invasive treatment for cerebral aneurysms and brain tumors *(3-4)*. In a typical embolization, a surgeon inserts a slender guidewire/catheter into the femoral artery of the patient and manually pushes/twists it to the target lesion in the brain through the blood vessels, followed by the delivery of embolic agents to block the target lesion *(5-7)*. For example, a surgeon delivers metallic coils (e.g., soft platinum) through the catheter to seal off the cerebral aneurysm, which stabilizes the aneurysm and minimizes the risk of rupture. Particulate (e.g., polyvinyl alcohol beads) is another common embolic agent in tumor embolization. As the catheter is pushed into the feeding vessels of a tumor, particles are delivered to cut off the blood supply to the tumor, starving the tumor for accelerated tumor removal *(8-15)*. However, current embolization by pushing/twisting a passive guidewire/catheter with a preshaped tip is often limited by its low steerability through complex vascular networks, i.e., the guidewire/catheter has a great challenge in turning to bifurcation branches of blood vessels. As a result, embolic agents may not be accurately delivered to the target lesion, leading to safety complications such as blockage of normal vessels. In addition, the surgeon suffers from the accumulated radiation when manually pushing/twisting the guidewire/catheter under the X-ray imaging. Therefore, there has been a high demand for a next-generation embolization technique with high steerability for targeted delivery of embolic agents and a remotely controllable operation for a radiation-free workplace.

Recently, active robots that can be remotely steered in the blood vessel have shown great promise in robotic embolization *(16-27)*. One widely used strategy is designing guidewire/catheter robots with an active tip that can bend in response to external stimuli such as hydraulic pressure *(19)*, electricity *(20)*, and magnetic fields *(21-25)*. For example, Kim *et al.* have developed a guidewire robot with a ferromagnetic tip that can bend by remotely applying magnetic fields *(22)*. Such an active guidewire robot has shown enhanced steerability in blood vessels and the capability of delivering embolic agents to an aneurysm *(23)*. However, maneuvering guidewires/catheters (regardless of passive and active tips) intrinsically requires tethered operation (e.g., pushing for advancement), which is of great difficulty when the slender guidewires/catheters are highly distorted, buckled, and looped in confined and tortuous blood vessels. This difficulty gets even more pronounced when the target lesion locates in the submillimeter regions. To address this issue, another strategy is to develop small-scale untethered robots that can navigate blood vessels as a substitute for guidewires/catheters. For example, flow-driven magnetic swarm *(28)*, magnetic particles *(29)*, and magnetic anchors *(30)* have been reported for potential application of tumor embolization in submillimeter regions. However, being passively carried by blood flow, these untethered robots lack reliable maneuverability for navigation in flow conditions, which may lead to severe complications of nontargeted embolization *(31-32)*. Although many other untethered robots (e.g., sheet-shaped magnetic robots and magnetic stents) have

shown improved navigation capability (e.g., adaptive locomotion) in flow conditions *(33-34)*, they have not been demonstrated for robotic embolization due to the limited shape-morphing ability at the target lesion. Therefore, to the best of our knowledge, there is no systematic study of active robots that demonstrates high steerability in tortuous blood vessels (especially in submillimeter regions), reliable maneuverability in flow conditions, and shape-morphing capability at target lesions (see Table S1).

Here, we present magnetic soft micro-fiber robots (hereafter referred to as micro-fiberbot) with enhanced steerability, reliable maneuverability, and shape reconfigurability to perform robotic embolization in a remotely controllable manner (Fig. 1A and Movie S1). Magnetic soft micro-fiberbots are in a helical geometry with a customizable diameter (denoted as D in Fig. 1B) that can be compatible with existing catheters to maximize their clinical effectiveness. A standard catheterization can be first performed by threading a commercial catheter through blood vessels until the intravascular advancement is stopped. Thereafter, the micro-fiberbots can be deployed into blood vessels through the catheter. Enabled by the contact friction, the micro-fiberbot can anchor to the blood vessel after deployment, without being flushed away by blood flow. By remotely applying magnetic fields, the micro-fiberbot can be actively steered in the blood flow (both upstream and downstream) via helical propulsion. The micro-fiberbots can be elongated for passing narrow regions and aggregated at the target lesion. The aggerated micro-fiberbot can either block the blood flow to the target aneurysm/tumor or protect the normal blood vessel, allowing for three embolization applications: aneurysm coil embolization, tumor coil embolization, and tumor particle embolization (Fig. 1A). We demonstrate both in vitro embolization of aneurysm and tumor in neurovascular phantoms and in vivo embolization of a rabbit femoral artery model under real-time fluoroscopy. As a supplement to conventional catheter-based embolization, our work presents a significant advancement for the minimally invasive treatment of cerebral aneurysms and brain tumors in a robotic setting.

RESULTS

Shape-morphing capability

The magnetic composite is first prepared by uniformly dispersing neodymium-iron-boron (NdFeB) microparticles in a thermoplastic matrix (poly (styrene-b-(ethylene-co-butylene)-b-styrene), SEBS)). The volume fraction of NdFeB is 20%. Using a thermal drawing technique (Fig. 1B and Fig. S1), straight magnetic micro-fibers with various diameters (denoted as d in Fig. 1C) are fabricated. By applying an impulse magnetic field (2.5T), the straight magnetic micro-fiber can be fully magnetized along the fiber direction. Thereafter, by coiling around a cylindrical mold and demolding after curing, the straight micro-fiber can be transformed into a magnetic soft micro-fiberbot with a helical magnetization **M** along its body. By changing the geometry of the cylindrical mold, the helical pitch p (Fig. 1B), and helical diameter D (Fig. 1D) of micro-fiberbots can be readily tuned. A representative micro-fiberbot with d= 60 μm, p = 800 μm, and D = 800 μm is selected for demonstrating embolization in submillimeter regions in this work (Fig. 1E).

When the micro-fiberbot reaches a vessel segment that has an inner diameter (denoted as H) slightly smaller than that of the micro-fiberbot, it will anchor to the blood vessel due to the contact friction, without being flushed away by the blood flow (Fig. 2A). Finite element simulation validates the total contact friction is larger than the fluidic drag force (Supplementary Text, Fig. S2). Despite the sufficient friction force, the maximum contact pressure with the vessel wall is as low as 4.3 kPa, which is much smaller than the threshold pressure for rupturing the blood vessel (12 kPa *(35-36)*). The helical magnetization profile

M endows the micro-fiberbot with a net magnetization (denoted as $\mathbf{M}_{net}$ in Fig. 2A) along its central axis. By applying an actuation magnetic field **B** that has the same direction as $\mathbf{M}_{net}$, the micro-fiberbot is elongated. The helical diameter gradually reduces as the magnetic field strength increases (Fig. S3). Conversely, when **B** is opposite to $\mathbf{M}_{net}$, the micro-fiberbot is aggregated (Fig. 2A and Movie S2) and its length gradually reduces as the magnetic field strength increases (Fig. S3). Such an aggregation/elongation shape-morphing is fully reversible even after 1000 cycles as validated by three micro-fiberbots with different pitches (Fig. S4). More impressively, the micro-fiber can still recover its helical shape even after a compression test under a rigid punch, manifesting a high elasticity and robustness (Fig. S5).

Magnetic maneuverability in flow conditions

Fig. 2B illustrates the strategy for magnetically maneuvering the micro-fiberbot in flow conditions. A cubic magnet (5×5×5 cm, residual magnetic flux density $\mathbf{B_r}$ = 1.38 T) is adopted as an actuation source (Fig. S6-S7). The magnet is manipulated by a 6-DoF robotic arm that can precisely control its current position denoted as (*x*,*y*) in the *xyz* coordinate system, axial rotation (rotating axis parallel with x-axis), and in-plane rotation (in *xy* plane)(Fig. S8). The rotating magnetic fields allow for high flexibility for manipulating untethered magnetic soft micro-fiberbot *(37)*. By axially rotating while moving the magnet leftward, we can maneuver the micro-fiberbot to the left via helical propulsion. Aside from high flexibility of control, such a helical propulsion motion is different from direct pulling mode by magnetic body force $\mathbf{f} = (\mathbf{M} \cdot \nabla)\mathbf{B}$ where a large magnetic field gradient $\nabla\mathbf{B} = [\partial\mathbf{B}/\partial x, \partial\mathbf{B}/\partial y, \partial\mathbf{B}/\partial z]^T$ is required *(38-40)*. When the micro-fiberbot reaches the target lesion, by rotation of 90° in the *xy* plane, we can generate a local actuation magnetic field **B** opposite to $\mathbf{M}_{net}$, leading to the aggregation shape morphing. If further magnetic pulling operation is needed, we can further rotate the magnet in the *xy* plane by 45° to generate a field gradient $\nabla\mathbf{B}$ as shown in Fig. S7. Therefore, the body force **f** will pull the micro-fiberbot to move with the magnet *(38)*. This magnetic pulling maneuvering will finally allow us to pull the aggregated micro-fiberbot to fill the aneurysm for embolization application. Corresponding actuation magnetic fields in each maneuvering process are shown in Fig. S6 and detailed magnetic maneuvering processes by the robotic arm equipped with a rotating permanent magnet are presented in Movie S3.

To validate the shape-morphing and magnetic maneuvering of the micro-fiberbot in flow conditions, we prepare a vessel phantom with an inner diameter H=800 μm and fill it with simulated blood (50% glycerol solution, viscosity 4 mPa·s). The flow rate is set as 100 mm/s via a pump system to mimic the typical blood flow in submillimeter regions of neurovascular networks *(41)*. We first show that the micro-fiberbot can stably anchor to the vessel in the absence of magnetic fields (Fig. 2C). By tuning the strength and the frequency of the rotating magnetic field, the helical propulsion velocity can be adjusted (Fig. S3C). If the simulated blood is not flowing, the helical propulsion velocity of the micro-fiberbot can reach up to 1.6 mm/s under a rotating magnetic field B=40 mT at a frequency of 5 Hz. When the flow rate is 100 mm/s, the upstream and downstream helical propulsion velocities of the micro-fiberbot change to 0.32 mm/s and 1.75 mm/s, respectively. It is also worth noting that the aggregated micro-fiberbot can also anchor to the blood vessel when the magnetic field is removed due to friction. This anchoring capability at the aggregated state allows the micro-fiberbot to be further pulled by applying a magnetic field gradient $\nabla\mathbf{B}$ that generates magnetic body force **f**. For example, by tuning the magnet's orientation of 45° in the *xy* plane, the aggregated micro-fiberbot can be further pulled inside the vessel (Fig. 2C). The helical shape of the micro-fiberbot is recovered when aligning the magnetic field **B** with a

net magnetization $\mathbf{M}_{net}$. It is also worth noting that such shape-morphing and propulsion capabilities may not be seriously affected by the size of the micro-fiberbot. We show that a micro-fiberbot with a 500 μm diameter still preserves comparable upstream propulsion velocity with that of the 800 μm micro-fiberbot in flow conditions up to 200 mm/s flow rate (Fig. S9, Movie S4).

Catheter-assisted deployment

Considering that there is a long way from the incision (usually at the femoral arteries) to the target lesion in the brain, our micro-fiberbot can be combined with existing medical catheters to reduce the operation time while increasing the embolization safety. Here, a representative medical catheter (MicroVention Terumo, tip inner diameter ID=0.027 inch (685 μm), distal outer diameter OD=2.6 F (866 μm), Fig. 1E) is selected for demonstrating the catheter-assisted deployment (Fig. 3). We show that the micro-fiberbot (D=800 μm) can be easily injected into the catheter via a 200 μm-needle syringe (Fig. 3A). Due to the elastic nature and high robustness, the highly coiled micro-fiberbot can quickly recover its helical shape after injection (less than 1s). In the absence of magnetic fields, perfusing saline into the catheter will push the micro-fiber to travel inside the catheter (since the diameter of the micro-fiberbot D is smaller than the inner diameter of the catheter H). When traveling inside the catheter, the micro-fiberbot can be readily tracked by X-ray imaging (Fig. 3B). Although the catheter cannot directly reach the target lesion, it still paves a safe way for the micro-fiberbot to approach the target lesion as close as possible. Thereafter, the micro-fiberbot will be remotely maneuvered by magnetic fields to complete the rest journey to the target lesion.

A blood vessel phantom with bifurcation branches (fabricated using a sacrificial template method, Fig. S10) is selected as an example (Fig. 3C, D). The mechanical properties (Young's modulus 2 MPa) and contact friction coefficient (0.1) are carefully tuned to mimic that of human blood vessels. Assume that the catheter can only reach the main blood vessel and two target lesions located on the bifurcation branches. To reach target 1, the micro-fiberbot can be released at the first bifurcation in the main vessel. Thereafter, the micro-fiberbot can be magnetically maneuvered to target 1 by helical propulsion, followed by on-demand aggregation. Similarly, to reach target 2, the catheter can be first threaded to the second bifurcation, and the micro-fiberbot is then released, magnetically steered, and aggregated at target 2. Detailed catheter-assisted deployment is shown in Movie S5. By combing with existing medical catheters, the clinical effectiveness of the micro-fiber can be maximized by reducing magnetic maneuvering, especially when multiple micro-fiberbots need to be deployed. In comparison, we show that without the micro-fiberbot, the catheter can only reach the second bifurcation. If coils are directly delivered at the second bifurcation, targeted embolization cannot be ensured (Fig. S11).

High steerability in submillimeter regions

The steerability of soft robots in blood vessels is often characterized by the angle of bifurcation branches and the diameter of the accessible blood vessel (see Table S1). To demonstrate the high steerability in submillimeter regions, we fabricate two phantoms of blood vessels (Fig. 4) with uniform diameter D= 800 μm. The first phantom has two bifurcation branches with angles of 30° and 60° (Fig. 4A), respectively, and the second phantom has two bifurcation branches with angles of 90° and 120° (Fig. 4B), respectively. It clearly shows that the micro-fiberbot can easily turn to the bifurcation branches of 30° via downstream helical propulsion. By reversely rotating the magnet, the micro-fiberbot can return via upstream helical propulsion. This reverse maneuvering implies that, if the micro-

fiberbot goes into a wrong branch vessel, it can be readily re-oriented to the right track. After that, the micro-fiberbot can be further maneuvered to a bifurcation branch vessel with 60°. In the second phantom, since the bifurcation angles are large, the micro-fiberbot needs to first turn its "head" into the branch vessel under a rotating magnetic field. Thereafter, a magnetic field **B** parallel to $\mathbf{M}_{net}$ is applied to stretch the micro-fiberbot, dragging it into the branch vessel. Once the whole body is steered to the bifurcation branches, the stretched micro-fiberbot quickly recovers its helical shape, continuing the helical propulsion in the branch vessel (Movie S6). In addition to the high steerability in large-angle bifurcation vessels, we further demonstrate that the micro-fiberbot can simply pass through a narrowing vessel with a minimum diameter of 100 μm in Fig. 4C and Movie S7. The micro-fiber is stretched by applying a parallel magnetic field so that it can pass the narrowing vessel with the flow. Considering that real blood vessels are three-dimensional (3D), we further present the steerability of the micro-fiberbot in an S-shaped (Movie S8) and 3D blood vessel phantom (Movie S9) in Fig. 4D and E, respectively. Both results show that the micro-fiberbot can be quickly steered through the blood vessel phantom. In contrast, we demonstrate that the commercial catheter cannot be directed to the bifurcation and narrowing branches as shown in Fig. S12.

In vitro demonstration of robotic embolization

To demonstrate the potential for treating cerebral aneurysms and brain tumors, we first perform robotic embolization demonstrations in submillimeter neurovascular vessel phantoms, which include aneurysm coil embolization (Fig. 5A, B), tumor coil embolization (Fig. 5C, D), and tumor particle embolization protection (Fig.5E-H). The first blood vessel phantom (H =800 μm) has a dilated aneurysm (Fig. 5A) and the second blood vessel phantom has three bifurcation branches with thinner diameters (H =500 μm) that are labeled as branch 1, branch 2, and branch 3, respectively (Fig. 5C-H). In aneurysm coil embolization, the micro-fiberbot is first helically propelled to the aneurysm and then transformed into the aggregated state. Via magnetic pulling, the aggregated micro-fiberbot can be pulled to fill the aneurysm (Fig. 5A and Movie S10). It is evident that the flow to the dilated aneurysm is significantly reduced after the aneurysm is filled (Fig. 5B). In tumor coil embolization, branch 2 is assumed to be tumor vessel while branch 1 and branch 3 are healthy blood vessels (Fig. 5C). A micro-fiberbot is first magnetically steered to branch 2 and aggregated. But it is found that only one aggregated micro-fiberbot cannot completely occlude branch 2 (Movie S11). Therefore, a second micro-fiberbot is deployed for a dual aggregation in branch 2. Compared with one aggregated micro-fiberbot, two aggregated micro-fiberbots significantly increase the blocking ratio (defined as the cross-sectional area of the micro-fiberbots divided by the blood vessel, Fig. S13) that almost blocks flow in branch 2 after embolization (Fig. 5D). Here, the dual aggregation is enabled by the independent actuation of each micro-fiberbot in sequence. As shown in Fig. S6, the rotating magnetic field for helical propulsion is zero along the $\mathbf{M}_{net}$ direction (i.e., Bx=0 in the *x*-direction), while elongation/aggregation requires Bx≠0. Therefore, when one micro-fiberbot is already aggregated at the target lesion, the magnetic field for helical propulsion of subsequent micro-fiberbots will not affect the already aggregated one, allowing for even quadruple-aggregation at the same target (Fig. S14) and occlusion at multiple blood vessel branches (Fig. S15 and Movie S12). In tumor particle embolization protection, branch 2 and branch 3 are assumed as tumor vessels while branch 1 is a healthy vessel (Fig. 5E). To prevent the embolic particles from flowing into healthy branch 1, a micro-fiberbot is first magnetically steered to branch 1 and aggregated. Then embolic particles (average diameter 250 μm) are released into the flow to selectively occlude branch 2 and branch 3 (Fig. 5F). Note that few particles may still be able to pass through the occluded area with one aggregated micro-

fiberbot. To achieve a large blocking ratio, dual aggregation can be performed, and the block ratio can reach up to 90% (Fig. S13). After the particle embolization is completed, the aggregated micro-fiberbot can be recovered and safely retrieved (Fig. 5G and Movie S13). It is confirmed that the tumor vessels (branch 2 and branch 3) are successfully occluded while the healthy vessel (branch 1) is perfectly protected (Fig. 5H).

In vivo demonstration of robotic embolization in a rabbit

We further demonstrate in vivo robotic embolization of a rabbit blood vessel on the right hind leg (diameter is from 500 μm to 800 μm) under real-time fluoroscopy (Fig. 6A). The micro-fiberbot is first injected into the femoral artery through a Terumo 2.6Fr catheter (Fig. 6B). The tortuous vessel is marked with 4 sites (Fig. 6C). Guided by fluoroscopic imaging (X-ray), the micro-fiberbot is helically propelled from site 1 to site 4 (Fig. 6D) and then returned to site 2 and eventually aggregated at site 2 (Fig. 6E and Movie S14). To validate the completed embolization, we then obtain the angiography of the femoral artery by injecting iodinated contrast media (Fig. 6F). Before embolization, we can see iodinated contrast media throughout the femoral artery, suggesting a normal flow in the artery. After embolization, no contrast media is observed due to the blockage of the flow by the aggregated micro-fiberbot (Fig. 6G and S16). The presence of the aggregated micro-fiberbot blocks the blood flow from the proximal to the distal end of the vessel, which leads to the formation of thrombosis inside the artery, as validated by the histological analysis two weeks after embolization (Fig. 6G, H). It is worth noting that no inflammation or pathological abnormalities are observed from the hematoxylin-eosin (H&E) staining results of the main organs including the lung, liver, spleen, kidney, and heart after two weeks (Fig. S17) and compared with an untreated control group, the levels of numbers of blood cells (RBCs, white blood cells, platelets, and lymphocytes) of robotic embolization procedure remained at normal levels after three weeks (Fig. S18), suggesting that the proposed robotic embolization by magnetically steering micro-fiberbots is safe.

DISCUSSION

Conventional embolization surgery by threading passive catheters to the target lesion is largely limited by the low steerability in complex blood vessels (especially in submillimeter regions) and accumulated radiation risk by manual operation. As a significant advancement, we develop magnetic soft micro-fiberbots that can perform embolization with high steerability by remotely controlling a 6-DoF robotic arm. With a helical magnetization along its body, the micro-fiberbot can be magnetically steered via helical propulsion in blood vessels and perform on-demand aggregation at the target lesion to occlude the blood flow. Using demonstration in submillimeter neurovascular vessel phantoms and in vivo rabbit femoral artery, we validate the potential for performing robotic embolization.

Our micro-fiberbots are still in their infancy, and we provide the following considerations for their clinical translation in the future. First, we have only demonstrated a micro-fiberbot with D = 800 μm for embolization in submillimeter blood vessels in this work. Actually, the helical diameter D of the micro-fiber can be effectively tuned by changing the geometry of the cylinder mold (Fig. 1B). If large aneurysms or blood vessels are encountered, micro-fiberbots with higher diameters may be selected. Also, we have shown that two aggregated micro-fiberbots can significantly enhance the blocking rate (Fig. S13), thus multiple micro-fiberbots can be deployed to the target lesion, if needed. Second, although the soft matrix of SEBS has been approved by U.S. Food and Drug Administration (FDA) for intravascular applications *(42)*, the ferromagnetic NdFeB particles may induce safety concerns for long-term implantation. In this regard, we can first coat a protective layer of pure SEBS shell by

thermal drawing technique (Fig. 1) and then dip coat a thin layer of hydrogel (15 μm) on the whole body of the micro-fiberbot to enhance biocompatibility and hemocompatibility (Fig. S19). This protection layers coating technique has been widely adopted to reduce the toxicity of the NdFeB-embedded composites *(22,23,34,43-45)*. According to the cell viability test and hemolysis assay, we show that the hydrogel skin can significantly reduce toxicity (cell viability 96%, Fig. S20) and hemolytic effect (hemolysis 1%, Fig. S21). Third, to realize the precise control of micro-fiberbots in tortuous blood vessels, an advanced positioning system is required. In addition to the fluoroscopy, we show that our micro-fiberbot can also be tracked using ultrasound imaging. An ex vivo demonstration in a porcine blood vessel is provided to validate the tracking capability under ultrasound imaging (Fig. S22). Other approaches such as photoacoustic computed tomography may also be helpful to obtain higher spatiotemporal resolution *(46)*. Last but not least, a faster thrombus formation is always desired for occluding the blood flow, leading to a successful embolization. In this regard, we present two potential solutions that have been reported in the literature for enhancing embolization efficiency. The first solution is to coat the micro-fiberbot with thrombin *(47)* such that blood cells can be absorbed onto the micro-fiberbot, as validated by the reduced blood clotting index and scanning electron microscope images in Fig. S22. The formed thrombus can resist a pressure of up to 22 kPa, which is large enough for blocking the blood flow in vivo (Fig. S23). The second solution is to further coat the micro-fiberbot with a thin functional layer (20 μm) of iron oxide (Fe_3O_4) nanoparticles that can generate heat upon radiofrequency (RF) stimulation (Fig. S19). By remotely heating the aggregated micro-fiberbot at the target lesion via RF coil (200 kHz), we can generate local hyperthermia that promotes thrombus formation. In vitro demonstration in the blood vessel phantom shows that a thrombus can be formed within 5 min (Fig. S24). The mechanism of local hyperthermia-induced thrombus formation lies in the activation and aggregation of platelets. When the temperature increases to about 41 ℃, platelets are activated in vivo and aggregated to form a thrombus. This mechanism has been widely reported in the literature *(48-51)* and is also validated by our experiments in which the activated coagulation time of the porcine blood decreases as the temperature rises from 37 to 50℃ (Fig. S26). In summary, we envisage that our magnetic soft micro-fiberbots will pave the way for the untethered robotic embolization of cerebral aneurysms and brain tumors in the future.

MATERIALS AND METHODS

Fabrication of magnetic soft micro-fiberbots. In the experiment, the ferromagnetic Neodymium Iron (NdFeB) particles with an average diameter of 5 μm were purchased from Guangzhou XND Co., Ltd., the soft elastomeric matrix styrene-ethylene-butylene-styrene (SEBS) materials (Kraton G1657) were purchased from KRATON Co., Ltd., the supporting polycarbonate (PC) pellets (Makrolon ET3113) was purchased from Covestro AG Co., Ltd. All materials were used as received. The ferromagnetic NdFeB particles were mixed in a pre-dissolved SEBS/Hexane solution (14.3 vol.%) with a volume ratio of 1:4 between NdFeB and SEBS. After mechanical stirring for 30 min and ultrasonic dispersing for 1 hr, the NdFeB/SEBS/Hexane suspensions were poured and doctor-bladed on PTFE films and dried in a fume hood for 10 hr. After fully dried, the resulting NdFeB/SEBS thin films were pealed from PTFE and cut into small slices of magnetic SEBS (M-SEBS). For M-SEBS core fabrication, the yielded M-SEBS slices were loaded in mold between a thermocompressor (Qien, Wuhan Qien Sci. & Tech. Co., Ltd.) and thermally pressed at 180℃ into M-SEBS cylinders. For supporting PC cladding fabrication, the fully dried PC pellets were loaded in mold between the thermocompressor and thermal pressed at 230℃ into cuboids. The PC cuboids were latterly lathed and drilled into PC tubes with an inner

diameter slightly larger than M-SEBS cylinders. The yielded M-SEBS cylinders were inserted into PC tubes for a monolithic preforms. The magnetic composites were prepared through the dispersion of unmagnetized magnetic microparticles (e.g., neodymium-iron-boron, NdFeB) in soft elastomeric matrix (e.g., poly (styrene-b-(ethylene-co-butylene)-b-styrene), SEBS) through chemical solution. Due to the limited drawability of the soft magnetic elastomer composite, we induced thermoplastic polycarbonate (PC) as sacrificial cladding for co-drawing. After thermal consolidation in a LEGO-like way, the preforms consisting of a magnetic soft core and sacrificial cladding were later thermally drawn into magnetic microfibers with different diameters (Fig. 1C) at 230℃ in a custom thermal draw tower.

Thermal drawing of magnetic microfibers. The resulting preforms consisted of M-SEBS core and PC cladding were thermally drawn into M-SEBS/PC fibers, referred to as magnetic fibers, at 230℃ in a custom thermal drawing tower. With a drawing ratio between 100 to 200, the diameter of magnetic fibers can be tuned between 20-90 μm. To enhance the functionality of micro-fiberbot, the functional layer was induced to the soft core perform. The performs consisting of a magnetic soft core (M-SEBs) and a functional layer (Fig. S19). The functional layer can be chosen according to different situations. For example, to enhance biocompatibility and hemocompatibility, a pure polymer protect layer can prevent corrosion of ferromagnetic particles (e.g. NdFeB). In addition, to enhance the embolization efficiency, a functional layer containing iron oxide (Fe_3O_4) nanoparticle can promote thrombus formation via RF heating.

Mechanical testing. The 80×80×2 mm M-SEBS thin film was cut into dumbbell test specimens using a standard part cutter. The mechanical testing was subjected to standard test methods (ASTM D412) on a mechanical testing machine at a displacement rate of 5 mm/s (width: 8 mm; gauge length: 60 mm).

Fabrication of magnetic soft micro-fiberbots. The magnetic microfibers were first magnetized by a 2.5 T impulse magnetic field generated by a digital pulse magnetizer (Beijing Eusci Technology Ltd). The fibers with PC cladding were then wrapped with identity helical parameters on a high thermal conductivity rod by tweezers. Adhesive tape was applied to ensure that the fiber was tightly contacted with the rod. The rod around with microfibers was then placed on a hot plate at 90°C for 30 min. After the magnetic microfiber was molded into helical-shaped structure, the robots were detached from the rods. sacrificial PC cladding was chemically selectively removed by N, N-Dimethylacetamide (Sinopharm Chemical Reagent Co., Ltd) until the cladding was completely dissolved. Finally, the robot was cut into desired structure parameters.

Ex vivo experiments under real-time ultrasound imaging. The medical imaging system compatibility of magnetic soft micro-fiberbot was demonstrated in a porcine coronary artery ex vivo under real-time ultrasound imaging. The porcine hearts were obtained from Shenzhen Advanced Medical Services Co. Ltd. A solution of glycerol (Sigma-Aldrich) in deionized water was used as a blood analog (Viscosity is 4 mPa·s) and the arteries were connected to a programmable pump (Longer Pump) to create the bloodstream (100 mm/s). The wireless portable ultrasound probe (SonoStar) with a maximum of 14 MHz was used for real-time guidance of the magnetic soft micro-fiberbot. After injection into the artery, the magnetic soft micro-fiberbot is magnetically actuated to swim with the flow to the targeted site. When the magnetic field was removed, the magnetic soft micro-fiberbot is anchored to the target blood vessel wall while withstanding the flow. The ultrasound

imaging in pulse repetition frequency mode verified the anchoring of the robot in dynamic flow. The magnetic soft micro-fiberbot is also magnetically actuated to swim against the flow and retrieved by a catheter inside the artery vessels.

Hydrogel skin fabrication. The dip-coating methods were used to create a hydrogel layer on the magnetic soft micro-fiberbot. The monomer of the hydrogel layer was acrylamide (AAm) (Sigma-Aldrich, A8887). The silane coupling agent was 3-(trimethoxysilyl) propyl methacrylate (TMSPMA). For 1 mL solution of AAm (2 moles per a liter of DI water, 2 mol L^{-1}), 1 µL of CTA (10% volume ratio in THF), 10 µL of acetic acid (0.1 moles per a liter of DI water, 0.1 mol L^{-1}), and 5.7 µL of TMSPMA are added, followed by vortex mixing for 60 s, and then 50 mg of Thrombin (2000 u/mg, Shanghai Yuanye Bio-Technology Co., Ltd.) was added. The bare magnetic fiber was treated with plasma within the 60 s to form the network of hydrophilic groups. The treated magnetic fiber was fixed to a home-made machine and immersed in the pre-gel solution (Fig. S23). Lastly, the hydrogel-coated microfiber is sealed in a bottle with saturated humidity and stored in an oven at room temperature for 24 h.

Cell toxicity assay. Human cardiac microvascular endothelial cell line was cultured and removed from the flask using enzymatic digestion (trypsin/EDTA). The cell suspension was centrifuged at 1000 rpm for 5 min. Resuspend the cell suspension in medium to adjust the density to 1×10^5 cells/ml. Use a multi-channel pipette to add 100 µL of medium to the peripheral wells of a 96-well tissue culture microtiter plate, and add 100 µL of cell suspension at a density of $1x10^5$ cells/ml to the remaining. Cells were incubated for 24 h (5% CO_2 at 37°C, >90% humidity) to exponential growth. The medium was aspirated after 24 h of incubation. To evaluate the cell toxicity of M-SEBS composites, 100 µL of the 100% of sample leaching solution including negative control, positive control, bare magnetic fiber, and hydrogel-coated magnetic fiber were added for treatment. Cells were incubated for another 48h (5% CO_2 at 37°C, >90% humidity). After removing the co-cultured material and replacing the medium, 10 µL CCK-8 solution (AR1199, Boster, China) was added to each wall, and the plate was placed on a microtiter plate photometer (Multiskan FC, Thermo Scientific) equipped with a 450 nm filter to measure the absorbance. The cell viability was calculated according to the following equation

$$\text{Cell viability (\%)} = \frac{C_{sample} - C_{blank}}{C_{control} - C_{blank}} \times 100\%$$

Where C_{sample} is the absorbance of sample, C_{sample} is the absorbance of control (without sample), C_{blank} is the absorbance of blank group.

Live/dead assay. Human cardiac microvascular endothelial cell line was cultured and removed from the flask using enzymatic digestion (trypsin/EDTA). The cell suspension was centrifuged at 1000 rpm for 5 min. 5 x 10^5 cells were inoculated in each well of a 6-well plate and incubated in a CO_2 incubator (5% CO_2 at 37°C, >90% humidity) for 24 hours to allow the cells to adhere to the wall. Subsequently, the medium was removed and 2 mL of the sample leaching solution from each group was added to the 6-well plate and incubation was continued for 48 hours. After washing the cells twice with PBS buffer, 0.5 mL of staining solution (KTA1001, Abbkine, China) was added to each well and incubated for 15 min at 37°C protected from light. After washing 2 more times with PBS, the cells were placed under a fluorescent microscope and photographed.

Hemolysis rate assay. 20 mL of newly collected immune blood (Shenzhen Advanced Medical Services Co. Ltd.) was added with 1 mL of 20 g/L potassium oxalate to prepare fresh anticoagulated immune blood. Take 8 mL of fresh anticoagulated rabbit blood and

dilute it with 10 mL of normal saline. Weigh 3 samples of 5 g each. After rinsing with tap water, rinse with distilled water, absorb the water with filter paper and put it in a test tube, add 10 mL of normal saline to each tube; for the negative control, add 10 mL of normal saline of the same batch number to each tube; for positive control, add 10 mL of distilled water to each tube. To evaluate the Hemolysis rate of M-SEBS composites, two groups including bare magnetic fiber and hydrogel-coated magnetic fiber were added 0.2 mL of diluted rabbit blood for treatment and placed in a 37°C water bath and continue to incubate for 60 min. Pour out the liquid in each tube and centrifuge for 5 min (2500 r/min). and the absorbance was measured with a spectrophotometer at a wavelength of 545 nm. The hemolysis rate was calculated according the following equation

$$\text{Hemolysis rate (\%)} = \frac{H_{sample} - H_{neg}}{H_{pos}} \times 100\ \%$$

Where H_{sample} is the absorbance at 545 nm of the sample, H_{neg} is the absorbance of negative group, and H_{pos} is the absorbance of positive group.

Blood clotting index test: First, 10 mg of pure hydrogel coating and thrombin hydrogel coating micro-fiberbot, was placed into the polypropylene dish, and pre-warmed at 37℃ for 5min. Second, 4.5 mL of fresh anti-coagulated porcine blood was added with 0.5 mL of 0.1 mol/L solution of Calcium Chloride to prepare fresh blood samples. Third, 100 μL of the blood was coated onto the materials immediately for 10 s. Then, 10 mL of deionized water was added to the dish and shaken at 50 rpm for 10 min to lyse RBCs that were not stuck in the clot. The absorbance of the resulting hemoglobin solution (sample) was measured at 540 nm by a MultiSkan microplate reader (Multiskan GO, Thermofisher scientific), and absorbance of 100 uL of clotted whole blood in 10 mL of deionized water was used as the control Finally, the Blood clotting index of different materials was calculated using the following equation:

$$\text{Blood clotting index (\%)} = \frac{S_{sample}}{S_{control}} \times 100\ \%$$

Preparation of RBC solution: A volume of 5 mL of fresh anti-coagulated porcine blood was taken into a blood centrifuge tube. RBCs were centrifuged at 200 g for 20 min at room temperature and the supernatant was gently removed. RBCs were washed three times with 500μl 1× PBS solution and finally resuspended with 500μl 1× PBS.

In vivo animal experiment setup.

The 8- to 10-week-old male New Zealand rabbits, weighing 1.5 to 2.0 kg, were obtained from Shenzhen Advanced Medical Services Co. Ltd. The ethical approval from the Institutional Animal Care and Use Committee was obtained prior to the research (AMS C2305004 R). The rabbit was anesthetized before the embolization procedure. The femoral artery is exposed through a small incision, and then the femoral artery is accessed using a standard 22-gauge needle and a 4-Fr sheath (Glidesheath, Terumo). Under fluoroscopic guidance (DSA, CGO-2100, Wandong), the iodinated contrast media is released to obtain the blood vessel frame and the magnetic soft micro-fiberbotwas gently injected into the artery through a 2.6-Fr catheter (Headway 27^{TM} microcatheter, Terumo). The rotating magnetic field was generated by a cubic NdFeB magnet (50 mm in diameter and 50 mm in height). The magnetic soft micro-fiberbots were reliable steered and navigated in a helical propulsion manner in the blood vessel. After the robot contracted into an aggregation state,

the magnetic field was removed and iodinated contrast media is gently released to obtain the angiography (See Fig.6). Then, the catheter and sheath were removed, and the wound was sutured. After two-week of post-surgery, tissue sections in embolization regions were prepared and stained with H&E for histological examinations.

Analysis and simulation. Magnetic fields around a cubic magnet are calculated using commercial software COMSOL Multiphysics 6.0. Finite element simulations of shape morphing of micro-fiberbot were conducted using commercial software ABAQUS/Standard 2017. The NdFeB embedded magnetic composite was modeled as the ideal hard-magnetic soft material with shear modulus 1 MPa and residual magnetization **M**= 120 kA/m. To account for the interaction between magnetic composite with embedded NdFeB particles and the external magnetic field **B**, we adopted a user element (UEL) subroutine based on the continuum framework *(52,53)*. The magnetic torque density $\boldsymbol{\tau}$ can be implemented by computing the magnetic Cauchy stress $\boldsymbol{\sigma}^{\mathbf{magnetic}} = -\mathbf{B}\otimes\mathbf{FM}$ where **F** is the deformation gradient and operator $\otimes$ represents a dyadic product that takes two vectors to yield a second-order tensor. The blood vessel is simplified as a rigid tube. The contact between the micro-fiberbot and the blood vessel is modeled as "Hard contact, No penetration" with a friction coefficient of 0.1. All simulations are checked with convergence.

Supplementary Materials

Movie S13. In vitro demonstration of particle embolization protection and retrieval.
Movie S14. In vivo demonstration of robotic embolization in a rabbit.

References and Notes

1. Y. Fan, X. Zhang, C. Gao, S. Jiang, H. Wu, Z. Liu, T. Dou, Burden and trends of brain and central nervous system cancer from 1990 to 2019 at the global, regional, and country levels. *Arch. Public Health* **80**, 209 (2022).
2. A. Burlakoti, J. Kumaratilake, J. Taylor, M. Henneberg, Relationship between cerebral aneurysms and variations in cerebral basal arterial network: a morphometric cross-sectional study in Computed Tomography Angiograms from a neurointerventional unit. *BMJ Open* **11**, e051028 (2021).
3. G. Toth, R. Cerejo, Intracranial aneurysms: Review of current science and management. *Vasc. Med.* **23**, 276-288 (2018).
4. J. J. Leyon, T. Littlehales, B. Rangarajan, E. T. Hoey, A. Ganeshan, Endovascular embolization: Review of currently available embolization agents. *Curr. probl. diagn. radiol*. **43**, 35-53 (2014).
5. B. S. Peters, P. R. Armijo, C. Krause, S. A. Choudhury, D. Oleynikov, Review of emerging surgical robotic technology. *Surg. Endosc*. **32**, 1636-1655 (2018).
6. Y. Fu, H. Liu, W. Huang, S. Wang, Z. Liang, Steerable catheters in minimally invasive vascular surgery. *Int. J. Med. Robot*. **5**, 381–391 (2009).
7. S. Gunduz, H. Albadawi, R. Oklu, Robotic devices for minimally invasive endovascular interventions: A new dawn for interventional radiology. *Adv. Intell. Syst.* **3**, 2000181 (2021).
8. J. Gould, Breaking down the epidemiology of brain cancer. *Nature* **561**, S40–S41 (2018).
9. R. Huang, J. Boltze, S. Li, Strategies for improved intra-arterial treatments targeting brain tumors: A systematic review. *Front. Oncol.* **10**, 1443 (2020).
10. A. I. Qureshi, V. Janardhan, R. A. Hanel, G. Lanzino, Comparison of endovascular and surgical treatments for intracranial aneurysms: An evidence-based review. *Lancet Neurol.* **6**, 816–825 (2007).
11. S. Juvela, K. Poussa, H. Lehto, M. Porras, Natural history of unruptured intracranial aneurysms: A long-term follow-up study. *Stroke* **44**, 2414–2421 (2013).
12. G. Guglielmi, F. Viñuela, G. Duckwiler, J. Dion, P. Lylyk, A. Berenstein, C. Strother, V. Graves, V. Halbach, D. Nichols, N. Hopkins, R. Ferguson, I. Sepetka, Endovascular treatment of posterior circulation aneurysms by electrothrombosis using electrically detachable coils. *J. Neurosurg.* **77**, 515–524 (1992).
13. S. Vaidya, K. R. Tozer, J. C. Chen, An overview of embolic agents. *Semin. Intervent. Radiol.* **25**, 204–215 (2008).
14. J. Hu, H. Albadawi, B. W. Chong, A. R. Deipolyi, A. Sheth, A. Khademhosseini, R. Oklu, Advances in biomaterials and technologies for vascular embolization. *Adv. Mater.* **31**, 1901071 (2019).
15. C. Y. Wang, J. Hu, R. A. Sheth, R. Oklu, Emerging embolic agents in endovascular embolization: An overview. *Prog. Biomed. Eng.* **2**, 012003 (2020).
16. B. J. Nelson, S. Gervasoni, P. W. Chiu, L. Zhang, A. Zemmar, Magnetically actuated medical robots: An in vivo perspective. *Proc. IEEE* **110**, 1028-1037 (2022).
17. H. Tillander, Magnetic guidance of a catheter with articulated steel tip. *Acta Radiol.* **35**, 62–64 (1951).
18. N. Gudino, J. A. Heilman, J. J. Derakhshan, J. L. Sunshine, J. L. Duerk, M. A. Griswold, Control of intravascular catheters using an array of active steering coils. *Med. Phys.* **38**, 4215–4224 (2011).
19. T. Gopesh, J. H. Wen, D. Santiago-Dieppa, B. Yan, J. S. Pannell, A. Khalessi, A. Norbash, J. Friend, Soft robotic steerable microcatheter for the endovascular treatment of cerebral disorders.

Sci. Robot. **6**, eabf0601 (2021).
20. M. F. Phelan, M. E. Tiryaki, J. Lazovic, H. Gilbert, M. Sitti, Heat-mitigated design and Lorentz force-based steering of an MRI-driven microcatheter toward minimally invasive surgery. *Adv. Sci.* **9**, 2105352 (2022).
21. L. Wang, D. Zheng, P. Harker, A. B. Patel, C. F. Guo, X. Zhao, Evolutionary design of magnetic soft continuum robots. *Proc. Natl Acad. Sci. U.S.A.* **118**, e2021922118 (2021).
22. Y. Kim, G. A. Parada, S. Liu, X. Zhao, Ferromagnetic soft continuum robots. *Sci. Robot.* **4**, eaax7329 (2019).
23. Y. Kim, E. Genevriere, P. Harker, J. Choe, M. Balicki, R. W. Regenhardt, J. E. Dmytriw, A. B. Patel, X. Zhao, Telerobotic neurovascular interventions with magnetic manipulation. *Sci. Robot.* **7**, eabg9907 (2022).
24. A. Azizi, C. C. Tremblay, K. Gagné, S. Martel, Using the fringe field of a clinical MRI scanner enables robotic navigation of tethered instruments in deeper vascular regions. *Sci. Robot.* **4**, eaax7342 (2019).
25. L. Pancaldi, P. Dirix, A. Fanelli, A. M. Lima, N. Stergiopulos, P. J. Mosimann, D. Ghezzi, M. S. Sakar, Flow driven robotic navigation of microengineered endovascular probes. *Nat. Commun.* **11**, 6356 (2020).
26. C. Chautems, A. Tonazzini, Q. Boehler, S. H. Jeong, D. Floreano, B. J. Nelson, Magnetic continuum device with variable stiffness for minimally invasive surgery. *Adv. Intell. Syst.* **2**, 1900086 (2019).
27. J. Hwang, J. Kim, H. Choi, A review of magnetic actuation systems and magnetically actuated guidewire- and catheter-based microrobots for vascular interventions. *Intell. Serv. Robot.* **13**, 1–14 (2020).
28. J. Law, X. Wang, M. Luo, L. Xin, X. Du, W. Dou, T. Wang, G. Shan, Y. Wang, P. Song, X. Huang, J. Yu, Y. Sun, Microrobotic swarms for selective embolization. *Sci. Adv.* **8**, eabm5752 (2022).
29. N. Li, F. Michaud, Z. Nosrati, D. Loghin, C. Tremblay, R. Plantefève, K. Saatchi, U. O. Häfeli, S. Martel, G. Soulez, MRI-compatible injection system for magnetic microparticle embolization. *IEEE Trans. Biomed. Eng.* **66**, 2331-2340 (2018).
30. Z. Li, Z. Chen, Y. Gao, Y. Xing, Y. Zhou, Y. Luo, W. Xu, Z. Chen, X. Gao, K. Gupta, K. Anbalakan, L. Chen, C. Liu, J. Kong, H. L. Leo, C. Hu, H. Yu, Q. Guo, Shape memory micro-anchors with magnetic guidance for precision micro-vascular deployment. *Biomaterials* **283**, 121426 (2022).
31. S. Gunduz, H. Albadawi, R. Oklu, Robotic devices for minimally invasive endovascular interventions: A new dawn for interventional radiology. *Adv. Intell. Syst.* **3**, 2000181 (2021).
32. J. I. Bilbao, A. Martínez-Cuesta, F. Urtasun, O. Cosín, Complications of embolization. *Semin. Intervent. Radiol.* **23**, 126–142 (2006).
33. Z. Ren, R. Zhang, R. H. Soon, Z. Liu, W. Hu, P. R. Onck, M. Sitti, Soft-bodied adaptive multimodal locomotion strategies in fluid-filled confined spaces. *Sci. Adv.* **7**, eabh2022 (2021).
34. T. Wang, H. Ugurlu, Y. Yan, M. Li, M. Li, A. M. Wild, E. Yildiz, M. Schneider, D. Sheehan, W. Hu, M. Sitti, Adaptive wireless millirobotic locomotion into distal vasculature. *Nat. Commun.* **13**, 4465 (2022).
35. D. Gonzalez-Rodriguez, L. Guillou, F. Cornat, J. Lafaurie-Janvore, A. Babataheri, E. de Langre, A. I. Barakat, J. Husson, Mechanical criterion for the ruptureof a cell membrane under compression. *Biophys. J.* **111**, 2711–2721 (2016).
36. E. A. G. Peeters, C. W. J. Oomens, C. V. C. Bouten, D. L. Bader, F. P. T. Baaijens, Mechanical and failure properties of single attached cells under compression. *J. Biomech.* **38**, 1685–1693 (2005).
37. A. W.,Mahoney, J. J. Abbott. Generating rotating magnetic fields with a single permanent magnet for propulsion of untethered magnetic devices in a lumen. *IEEE Trans. Robot.*, **30**, 411-

420(2013)
38. J. J. Abbott., E.Diller, A. J.Petruska. Magnetic methods in robotics. *Annu. rev. control robot. auton. syst.*, **3**, 57-90 (2020)
39. B. Wang, K. F. Chan, K. Yuan, Q. Wang, X. Xia, L. Yang, H. Ko, Y.-X. J. Wang, J. J. Y. Sung, P. W. Y. Chiu, L. Zhang, Endoscopy-assisted magnetic navigation of biohybrid soft microrobots with rapid endoluminal delivery and imaging. *Sci. Robot.* **6**, eabd2813 (2021).
40. Q. Wang, X. Du, D. Jin, L. Zhang, Real-Time Ultrasound Doppler Tracking and Autonomous Navigation of a Miniature Helical Robot for Accelerating Thrombolysis in Dynamic Blood Flow. *Acs Nano*, **16**, 604-616 (2022).
41. L., Zarrinkoob, K.,Ambarki, A., Wåhlin, R., Birgander, A., Eklund, & J., Malm, Blood flow distribution in cerebral arteries. *J. Cereb. Blood Flow Metab.* **35**, 648-654. (2015).
42. U.S. Food and Drug Administration (FDA), *Class 2 medical device recalls: Swan-Ganz Catheters* (510(K) Number: K193466, FDA, 2020); https://www.accessdata.fda.gov/scripts/cdrh/cfdocs/cfPMN/pmn.cfm?ID=K193466
43. W. Hu, G. Z. Lum, M. Mastrangeli, M. Sitti, Small-scale soft-bodied robot with multimodal locomotion. *Nature* **554**, 81-85 (2018).
44. C. Zhou, Y. Yang, J. Wang, Q. Wu, Z. Gu, Y. Zhou, X. Liu, Y. Yang, H. Tang, Q. Ling, L. Wang, J. Zang, Ferromagnetic soft catheter robots for minimally invasive bioprinting. *Nat. Commun.*, **12** (2021).
45. Y. Yang, J. Wang, L. Wang, Q. Wu, L. Ling, Y. Yang, S. Ning, Y. Xie, Q. Cao, L. Li, J. Liu, Q. Ling, J. Zang, Magnetic soft robotic bladder for assisted urination. *Sci. Adv.*, **8**, q1456 (2022).
46. Z. Wu, L. Li, Y. Yang, P. Hu, Y. Li, S. Y. Yang, L. V. Wang, W. Gao, A microrobotic system guided by photoacoustic computed tomography for targeted navigation in intestines in vivo. *Sci. Robot.* **4**, eaax0613 (2019).
47. D. A.,Nicholson, J. F.,Cockburn, A. E.,Bradshaw, P. Dawson.. Thrombin-soaked embolization coils: The effect on whole blood clotting time. *Clin. Radiol.*, **46**, 108-110 (1992)
48. G.,Lippi, M., Franchini, G,Targher. Arterial thrombus formation in cardiovascular disease. *Nat. Rev. Cardiol.*, **8**, 502-512 (2011)
49. S. V.,Strother, J. M.,Bull, & S. A., Branham. Activation of coagulation during therapeutic whole body hyperthermia. *Thromb. Res.*, **43**, 353-360 (1986)
50. T., Iba, J., Helms, M., Levi, & J. H., Levy. The role of platelets in heat-related illness and heat-induced coagulopathy. *Thromb. Res.* (2022)
51. O. Suzuki, S. Miyachi, T. Okamoto, A. Ito, M. Shinkai, H. Honda, T. Kobayashi, M. Negoro, J. Yoshida. Local hyperthermia enhances thrombosis in aneurysms containing platinum coils. *Interv. Neuroradiol.*, **10**, 203-211 (2004)
52. L. Wang, Y. Kim, C. F. Guo, X. Zhao, Hard-magnetic elastica. *J. Mech. Phys. Solids* **142**, 104045 (2020).
53. R. Zhao, Y. Kim, S. A. Chester, P. Sharma, X. Zhao. Mechanics of hard-magnetic soft materials. *J. Mech. Phys. Solids* **124**, 244-263 (2019).

Acknowledgments: We thank others for any contributions.

Funding: This work was supported by the National Natural Science Foundation of China (51572096, 51820105008,11272369).

Author contribution: J.Z., G.T., G.-Z.Y., and X.L. conceived the idea and designed the research. X.L. and Y.X. performed the thermal drawing experiments. X.L. and F.L constructed the experimental platform. X.L., F.L, N.L., performed other experiments and analyzed the data. L.W.

and X.L. performed the theoretical analysis and numerical calculations. X.L., L.W, Y.X., G.-Z.Y., G.T. and J.Z. wrote the manuscript with input from all authors. All authors participated in drafting the manuscript, discussing, and interpreting the data.

Competing interesting: J.Z. and X.L. have a provisional patent application on the fundamental principles and designs of transforming untethered magnetic soft micro-fiberbot for endovascular intervention. The other authors declare that they have no competing financial interests.

Data and materials availability: All data are available in the main text or the supplementary materials.

Figures:

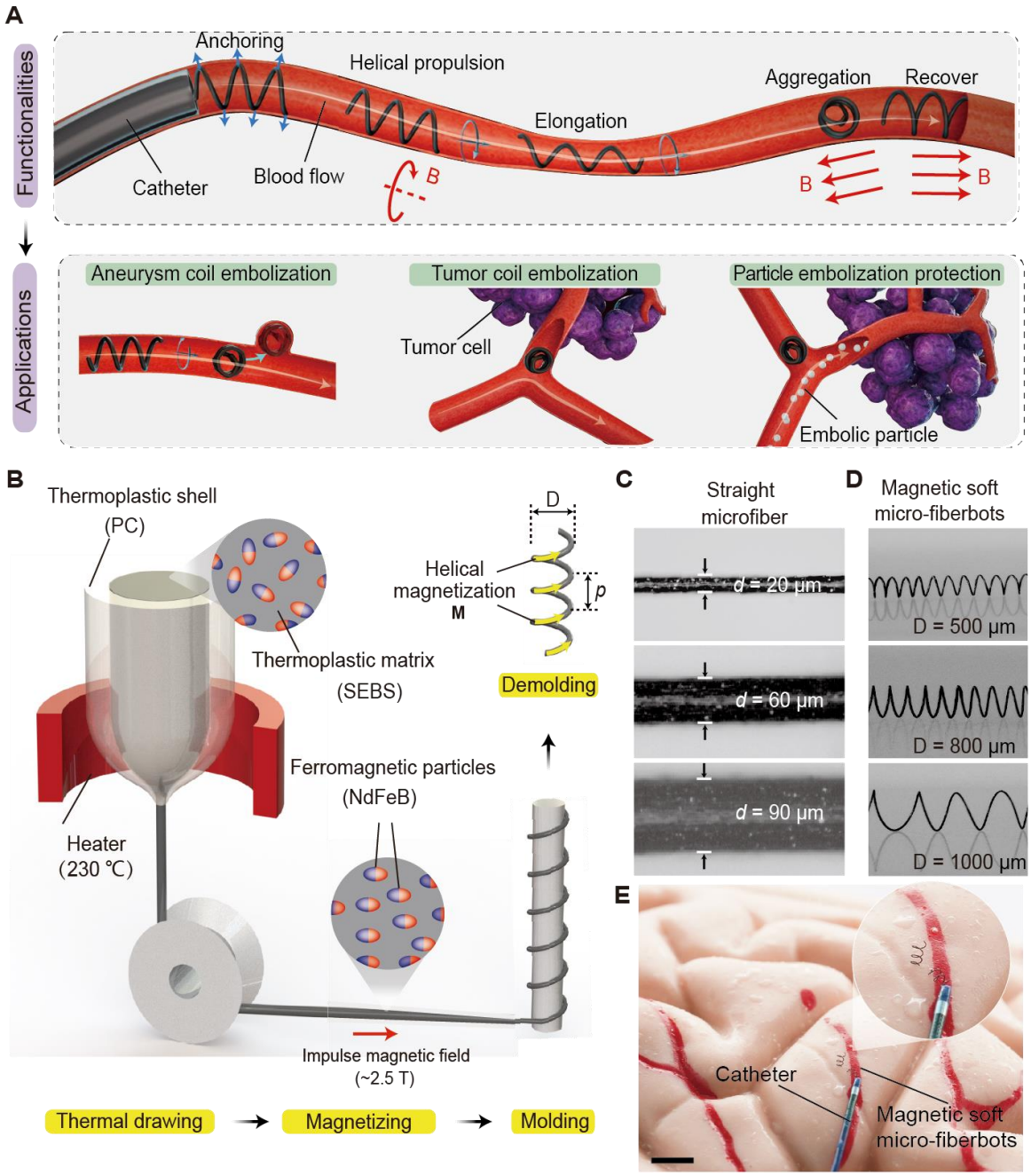

Fig. 1. **Magnetic soft micro-fiberbots for robotic embolization**. **A,** Schematic illustration of functionalities and potential applications of magnetic soft micro-fiberbots. The micro-fiberbot can anchor to a blood vessel after being released, navigate inside the blood flow via helical propulsion, pass through narrow regions by elongation, and block the blood flow by aggregation. The aggregated micro-fiberbots can be used as embolic agents for coil embolization of aneurysms and tumors, as well as a protection device for selective particle embolization of tumors. **B**, Fabrication process of magnetic soft micro-fiberbots: thermal drawing of magnetic soft micro-fiber, magnetizing by a strong impulse magnetic field (2.5 T), and molding/demolding into a helix shape. **C**, Optical imaging of magnetic soft micro-fibers with different fiber diameters denoted as *d*. **D**, Optical images of magnetic soft micro-fiberbots with different helical diameters denoted as D. Scale bar, 1mm. **E**, An image of magnetic soft micro-fiberbots deployed via Terumo 2.6Fr catheter to the surface of the brain phantom. Scale bar, 5 mm.

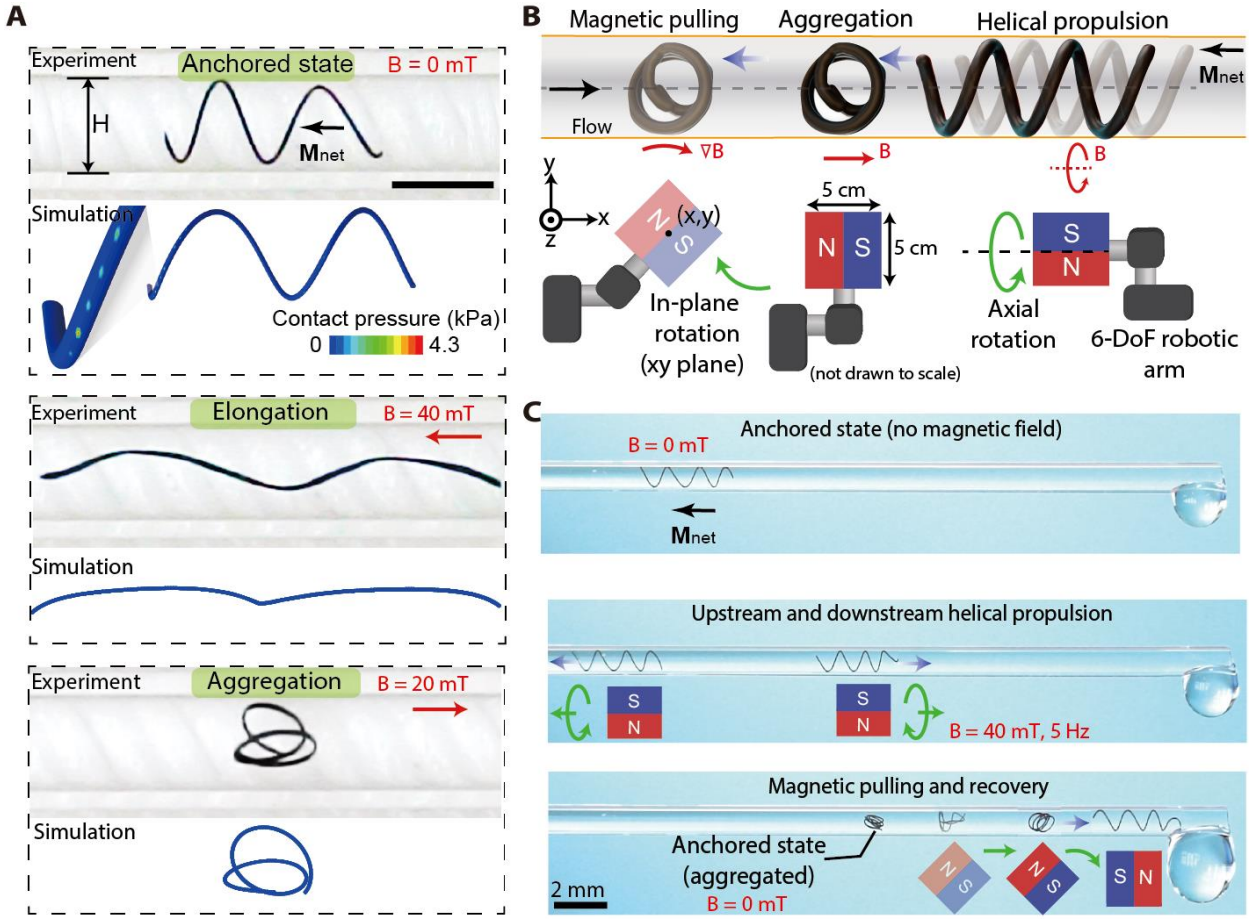

Fig. 2. Shape-morphing capability and magnetic maneuverability in flow conditions. A, The micro-fiberbot can anchor to the vessel in the absence of magnetic fields. By further applying static magnetic field **B** parallel to its net magnetization (denoted as $\mathbf{M}_{net}$), the magnetic soft micro-fiberbot can have reversible elongated and aggregated states. Scale bar, 1 mm. **B**, Schematic illustration of manipulating the micro-fiberbot by controlling a cubic magnet with a 6-DoF robotic arm. The helical propulsion is enabled by axially rotating the magnet (rotating axis is parallel with x-axis), while magnetic pulling is enabled by rotating magnet in the *xy* plane. **C**, Experimental pictures show that the micro-fiberbot (d = 60 um, p = 800 um, and D = 800 um) can steadily anchor to a vessel phantom (inner diameter H = 800 μm) in the absence of magnetic fields, upstream/downstream helical propulsion under rotating magnetic fields (B = 40 mT, frequency 5 Hz), and magnetic pulling under magnetic field gradient and recover to the helical shape.

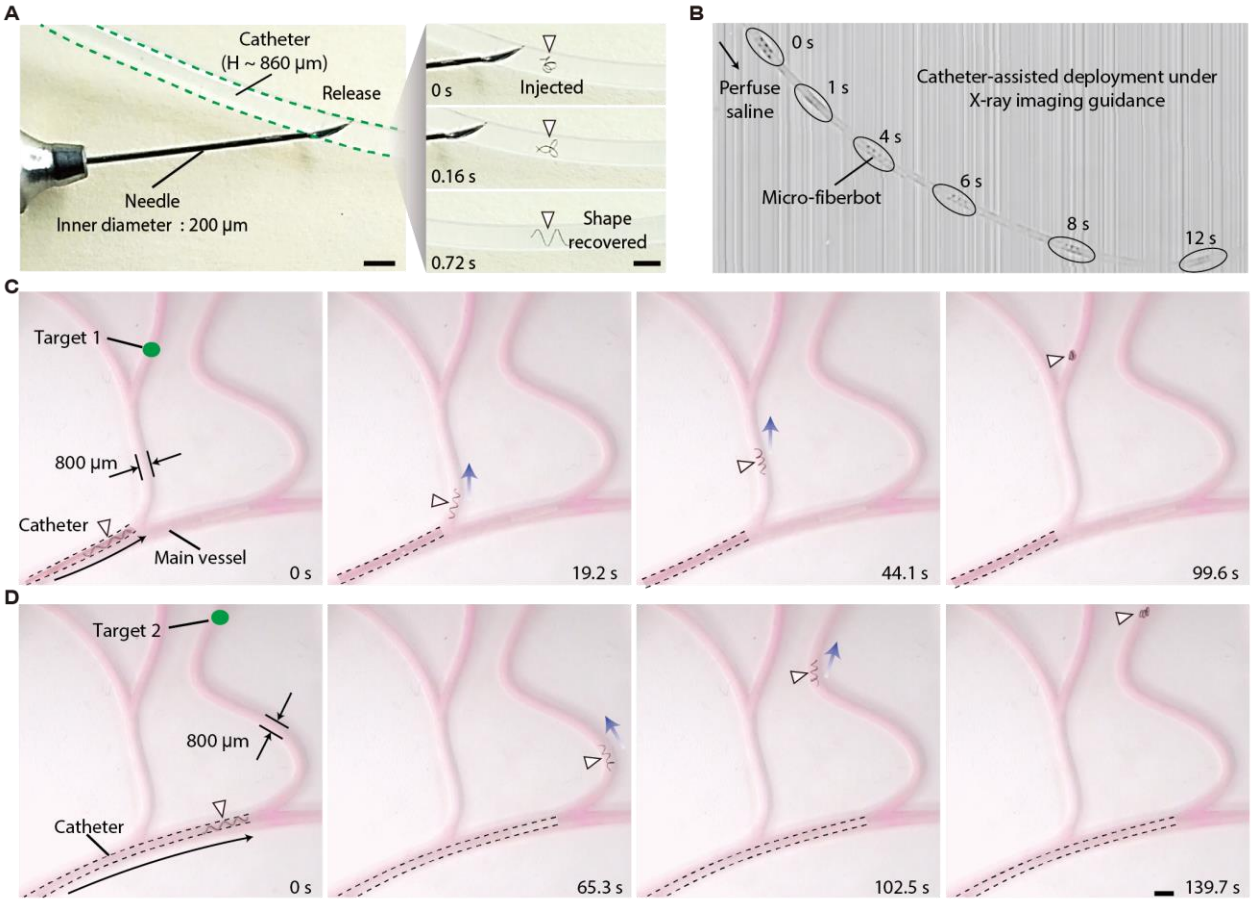

Fig. 3. Catheter-assisted deployment of the micro-fiberbot. A, The micro-fiberbot can be injected into a commercial catheter with a micro-needle syringe. The micro-fiberbot quickly recovers its helical shape after injection. **B**, The micro-fiberbot travels inside the catheter by perfusing saline under X-ray imaging guidance. **C-D**, Catheter-assisted deployment of the micro-fiberbot for embolization at target 1 (C) and target 2 (D) in a blood vessel phantom with bifurcation branches.

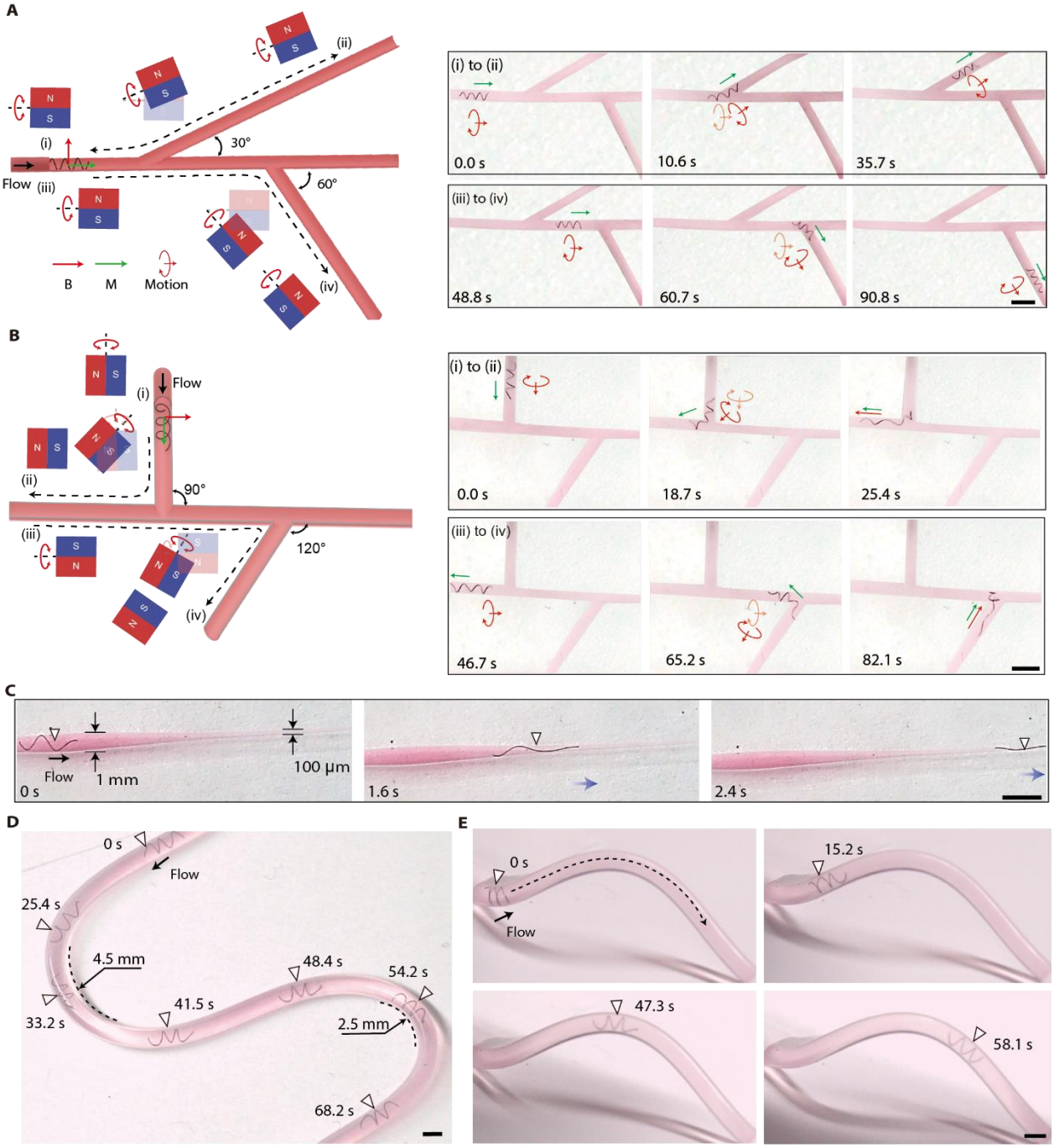

Fig. 4. Steerability of the micro-fiberbot in submillimeter regions. A, Schematic illustration (left) and experimental demonstration (right) of the micro-fiberbot navigating in a blood vessel phantom with bifurcation branches of 30° and 60°. **B**, Schematic illustration (left) and experimental pictures (right) of the micro-fiberbot navigating in a blood vessel phantom with bifurcation branches of 90° and 120°. **C**, Experimental demonstrations of the micro-fiberbot navigating in a vessel phantom with a narrowing diameter (1 mm to 100 µm). Scale bar, 2 mm. **D**, Demonstration of the micro-fiberbot navigating a S-shaped vessel phantom. **E**, Demonstrations of the micro-fiberbot navigating a 3D vessel phantom. Scale bar in D-E, 1 mm.

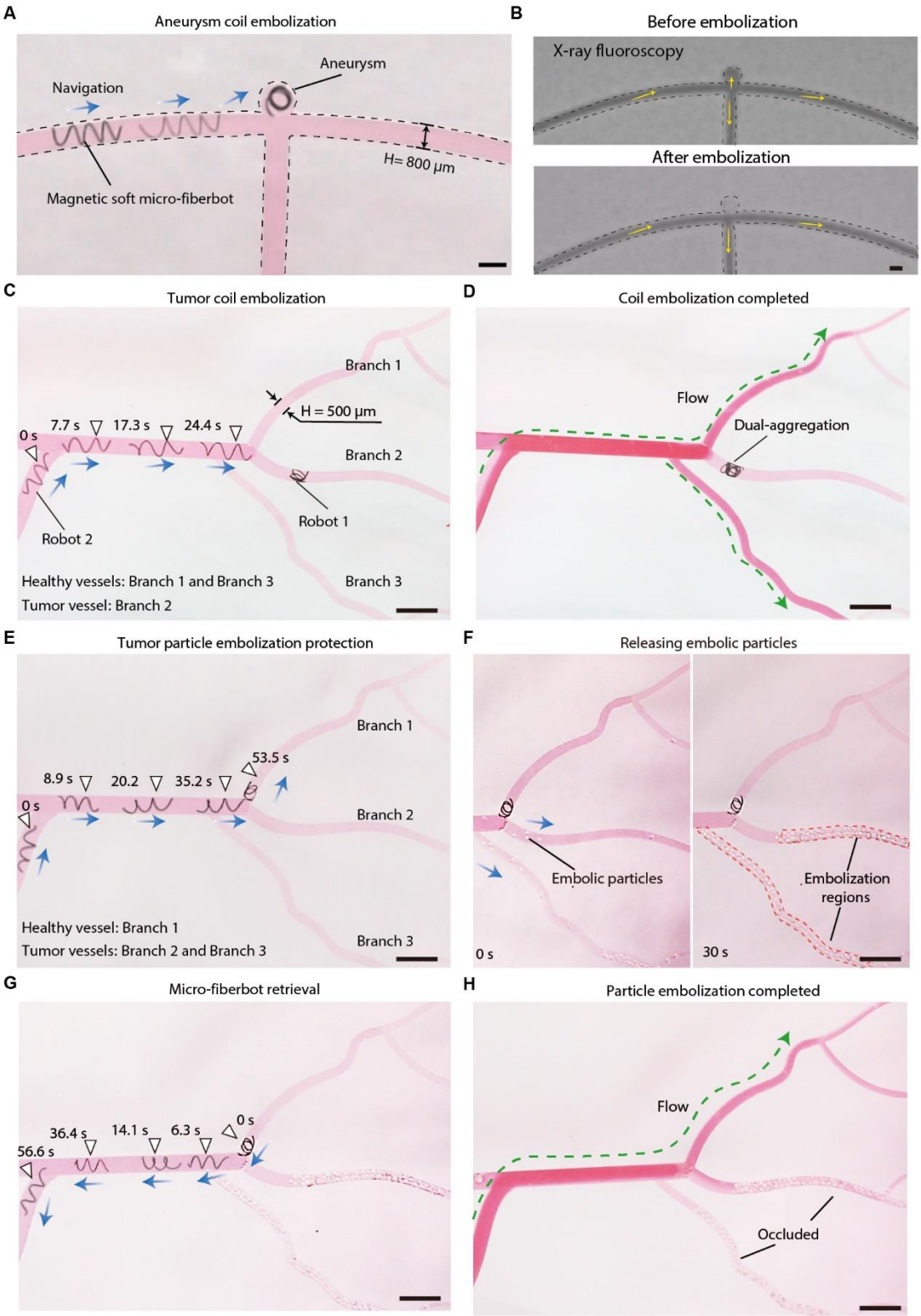

Fig. 5. In vitro robotic embolization in neurovascular vessel phantoms. A, Demonstration of aneurysm coil embolization by magnetic soft micro-fiberbot. **B,** Validation of the embolization results under X-ray fluoroscopy. The flow into the aneurysm is significantly reduced after coil embolization. **C**, Demonstration of tumor coil embolization in which branch 2 is assumed to be tumor vessel. Two micro-fiberbots are steered subsequently to completely occlude branch 2. **D**, The contrast agent is released to validate the occluded branch 2. **E**, Demonstration of tumor particle embolization protection in which branch 1 is assumed to be a healthy vessel. **F**, After the micro-fiberbot block the healthy branch 1, the embolic particles are released to occlude tumor vessels

(branch 2 and 3). **G,** The micro-fiberbot can be safely retrieved after particle embolization is completed. **H,** The contrast agent is released to validate the occluded vessel branch 2 and 3. Scale bar in A-H is 1 mm.

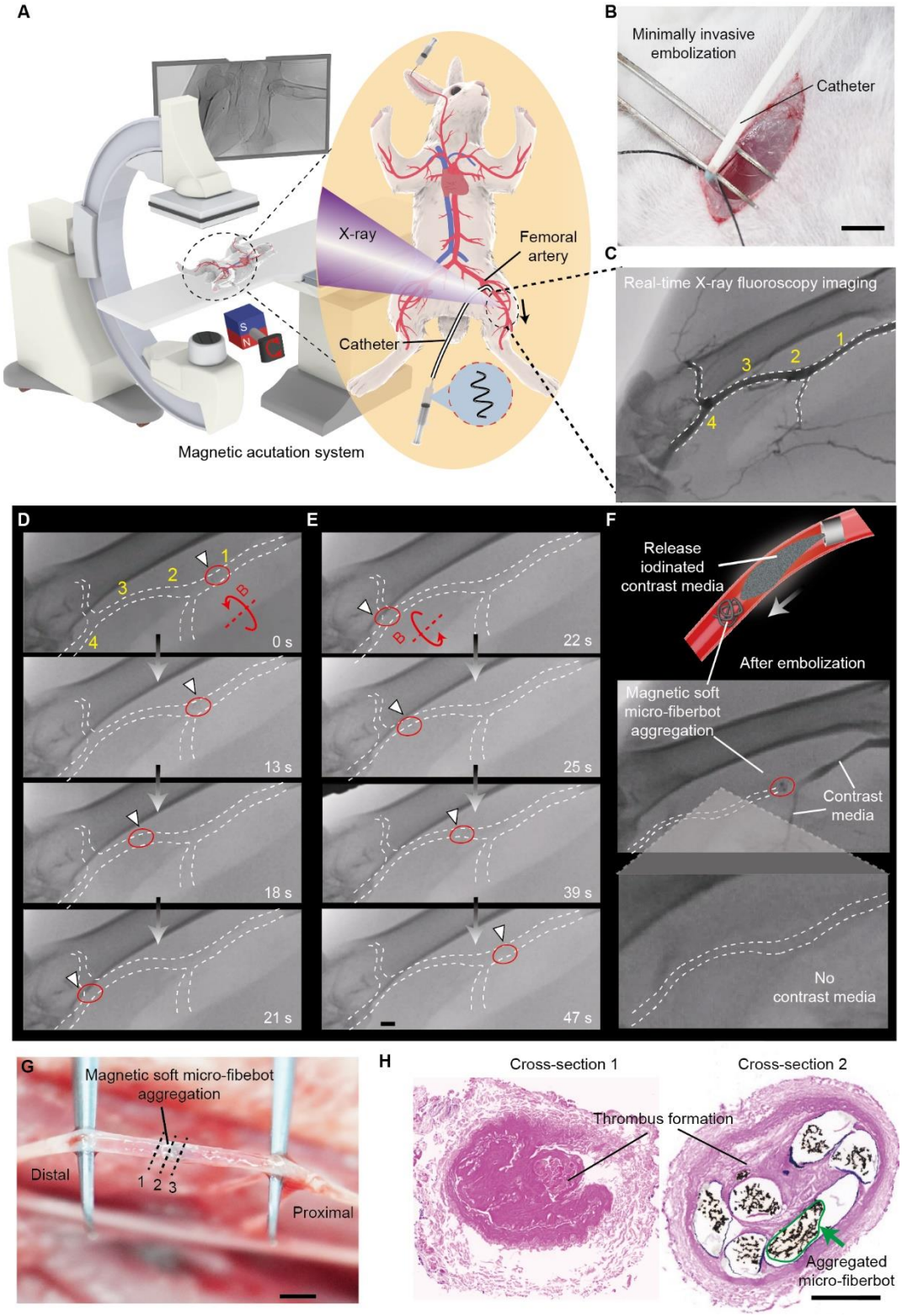

Fig.6. Robotic embolization in rabbit blood vessel in vivo. A, Schematic illustration of robotic embolization in rabbit blood vessel on the leg under real-time fluoroscopy. **B**, The magnetic soft micro- fiberbot is released into the blood vessel by a catheter. Scale bar, 5 mm. **C,** The angiology of targeted blood vessel before embolization by infusing iodinated contrast media. **D**, Fluoroscopy images of micro-fiberbot navigating from site 1 to site 4. **E**, Fluoroscopy images of micro-fiberbot returning from site 4 to site 2 and aggregated. **F**, The angiology of blood vessel after embolization by infusing iodinated contrast media. Scale bar, 1 mm. **G**, The blood vessel is separated for

histological analysis two weeks after embolization. Scale bar, **D-G**, 1 mm. **H,** The H&E staining cross-section images of the blood vessel. Cross-section 1 and 2 show the formation of thrombus after embolization. Scale bar, 250 μm.

Science Robotics

AAAS

Supplementary Materials for

Magnetic soft micro-fiberbots for robotic embolization

Xurui Liu[1,2]†, Liu Wang[3]†, Yuanzhuo Xiang[2]†, Fan Liao[1,2], Na Li[1, 2], Jiyu Li[3], Jiaxin Wang[4], Qingyang Wu[1, 2], Cheng Zhou[1, 2], Youzhou Yang[1, 2], Yuanshi Kou[1, 2], Yueying Yang[1, 2], Hanchuan Tang[1, 2], Ning Zhou[4], Chidan Wan[5], Guang-Zhong Yang[6]*, Guangming Tao[2, 7]*, Jianfeng Zang[1, 2, 8]*

†These authors contributed equally to this work.

*Corresponding authors. Email: gzyang@sjtu.edu.cn (G.-Z.Y.); tao@hust.edu.cn (G.T.); jfzang@hust.edu.cn (J.Z.);

This PDF file includes:

Other Supplementary Materials for this manuscript include the following:

Supplementary Text

Analysis of the anchored state of micro-fiberbot in flow conditions.

The flow velocity distribution inside a cylindrical vessel can be expressed*(1-3)*

$$v_r = f(r, H)v_m \quad \text{Eq. S1}$$

where H is the diameter of the vessel, r denotes the position with respect to the cylinder center O, and the mean flow velocity v_m. Considering that the diameter of the fiber (d = 60 μm) is much smaller than the vessel diameter (H = 800 μm), the position of the anchored micro-fiberbot can be estimated as

$$r = (H - d)/2. \quad \text{Eq. S2}$$

In a flow condition with $v_m = 100$ mm/s, Plugging Eq. S2 into Eq. S1 gives the flow velocity at the micro-fiberbot

$$v_r = 15 \text{ mm/s} \quad \text{Eq. S3}$$

Therefore, the fluidic drag force applied on one pitch of the micro-fiberbot can be estimated as

$$F_d = \frac{1}{2}\xi\rho S v_r \quad \text{Eq. S4}$$

where ξ is the drag coefficient, ρ is the flow density, S is the cross-section area of the micro-fiberbot. Substituting ξ = 0.15*(4)*, $\rho = 1.11 \times 10^3$ kg/m^3, $S = 2.9 \times 10^{-6}$ mm^2 into Eq. S4, we obtain that $F_d = 5.43 \times 10^{-7}$ N. According to the FEA, the total contact friction $F_f = 2.03 * 10^{-6}$ N.

Table. S1. Comparison between this work and existing embolization procedure

Strategy		Target indication	Embolic agent type	Embolic agent deployment technique	Steerability (max bifurcation angle θ, min diameter of accessible vessels H)	Maneuverability in flow conditions	Shape-morphing capability	Embolization Validation	Ref.
Commercial passive catheters		Aneurysm and tumor	Coil	Manually pushing/twisting guidewire to target lesions, followed by catheter delivery	Low $\theta < 90^\circ$ $H \sim 1$ mm	Intermediate (Buckled/looped in tortuous blood vessels)	Bending only	Commercial	**Catheter:** TERUMO Headway 27™ **Coil:** Stryker, Target™ Nano™
Active robots	Tethered hydraulic catheters	Aneurysm	Coil		Intermediate $\theta > 90^\circ$ $H \sim 2.5$ mm			In vivo (porcine)	*5*
	Tethered electronic catheters	Aneurysm	Coil		Low $\theta > 90^\circ$ $H \sim 2.5$ mm			In vitro	*6*
	Tethered magnetic guidewire	Aneurysm	Coil		Intermediate $\theta > 90^\circ$ $H \sim 2.5$ mm			In vitro	*7*
	Tethered magnetic catheter	Tumor	Liquid embolic	Catheter-directed to blood vessel & passively carried by blood flow & passively aggregate at target lesions	Intermediate $\theta < 90^\circ$ $H \sim 100$ μm	Intermediate (Impractical in unpredictable flow conditions)		Ex vivo	*8*
	Flow-driven swarms	Tumor	Particle		High (theoretically can steer to submillimetre regions due to the micro-size)	Low (Untraceable & passive drifted)	Particle aggregation	In vivo (porcine)	*9*
	Flow-driven particles	Tumor	Particle					In vitro	*10*
	Flow-driven anchors	Tumor	Particle				Radial expansion	In vivo (rabbit)	*11*
	Magnetic soft micro-fiberbots	**Aneurysm and tumor**	**Coil and particle**	**Catheter-directed to blood vessel & active navigation in blood flow & shape-morphing at target lesions**	**High** **$\theta > 90^\circ$** **$H \sim 100$ μm**	**High (controlled by magnetic fields & visible to X-ray/ultrasound)**	**Elongation, contraction, aggregation**	**In vivo** (rabbit)	**This work**

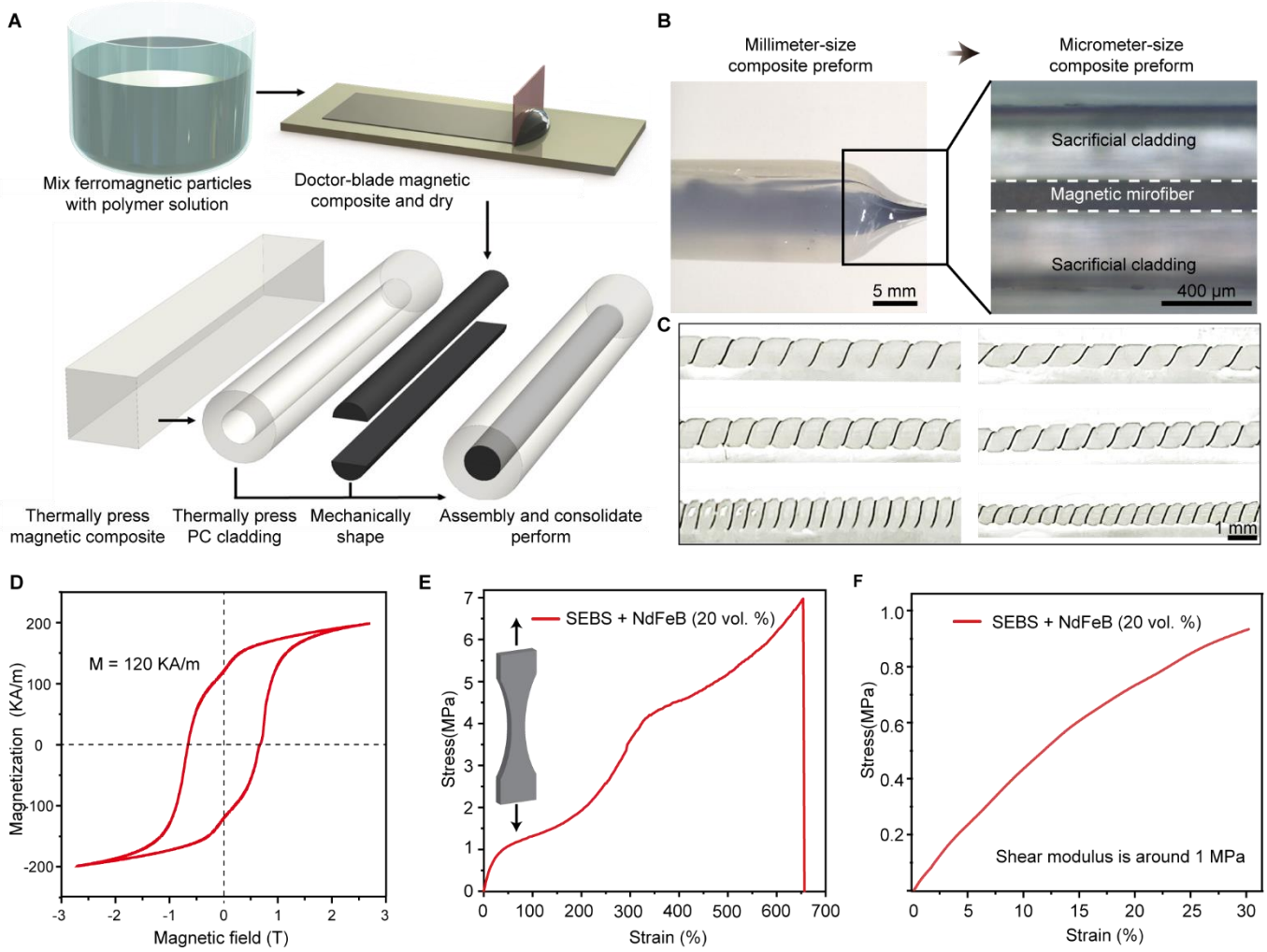

Fig. S1. Fabrication and characterization of magnetic soft micro-fiberbots. A, Schematic of fabrication of millimeter-scale magnetic composite preform. **B,** A millimeter-scale perform is thermally drawn into a micrometer-size perform with sacrificial PC cladding and magnetic microfiber core. **C,** the magnetic fiber can be molded into magnetic soft micro-fiberbots with identified helical geometry parameters by employing different molds. **D,** Magnetic hysteresis of SEBS+NdFeB (20 vol.%) composite. Residual magnetization **M**=120 kA/m. **E,** Stress-strain curves of SEBS+NdFeB (20 vol.%) composite. **F,** Fitting the stress-strain curve by the incompressible neo-Hookean constitutive model (Shear modulus is 1 MPa).

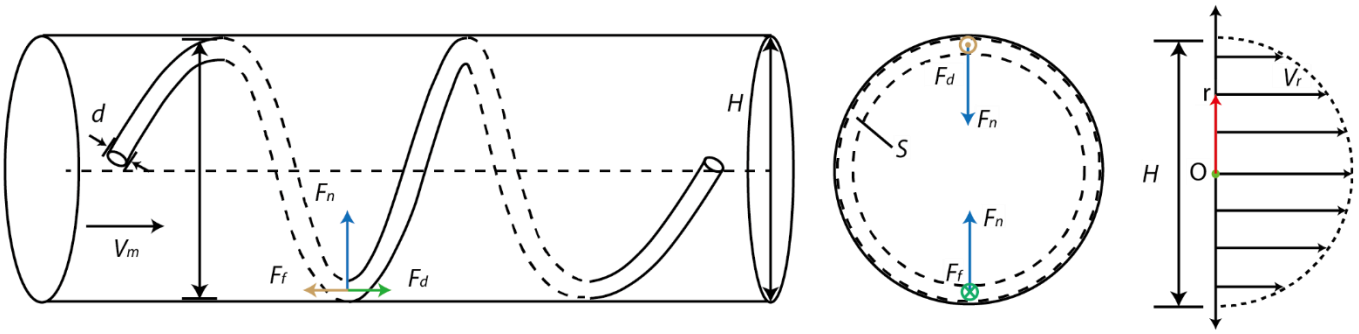

Fig. S2. Analysis of the anchored state of micro-fiberbot in flow conditions. The fluidic drag force (per pitch) F_d is estimated by the drag pressure times the cross-sectional area of the micro-fiber ($S = \pi\left(\frac{H^2}{4} - \frac{\left(\frac{H}{2}-d\right)^2}{4}\right)$).

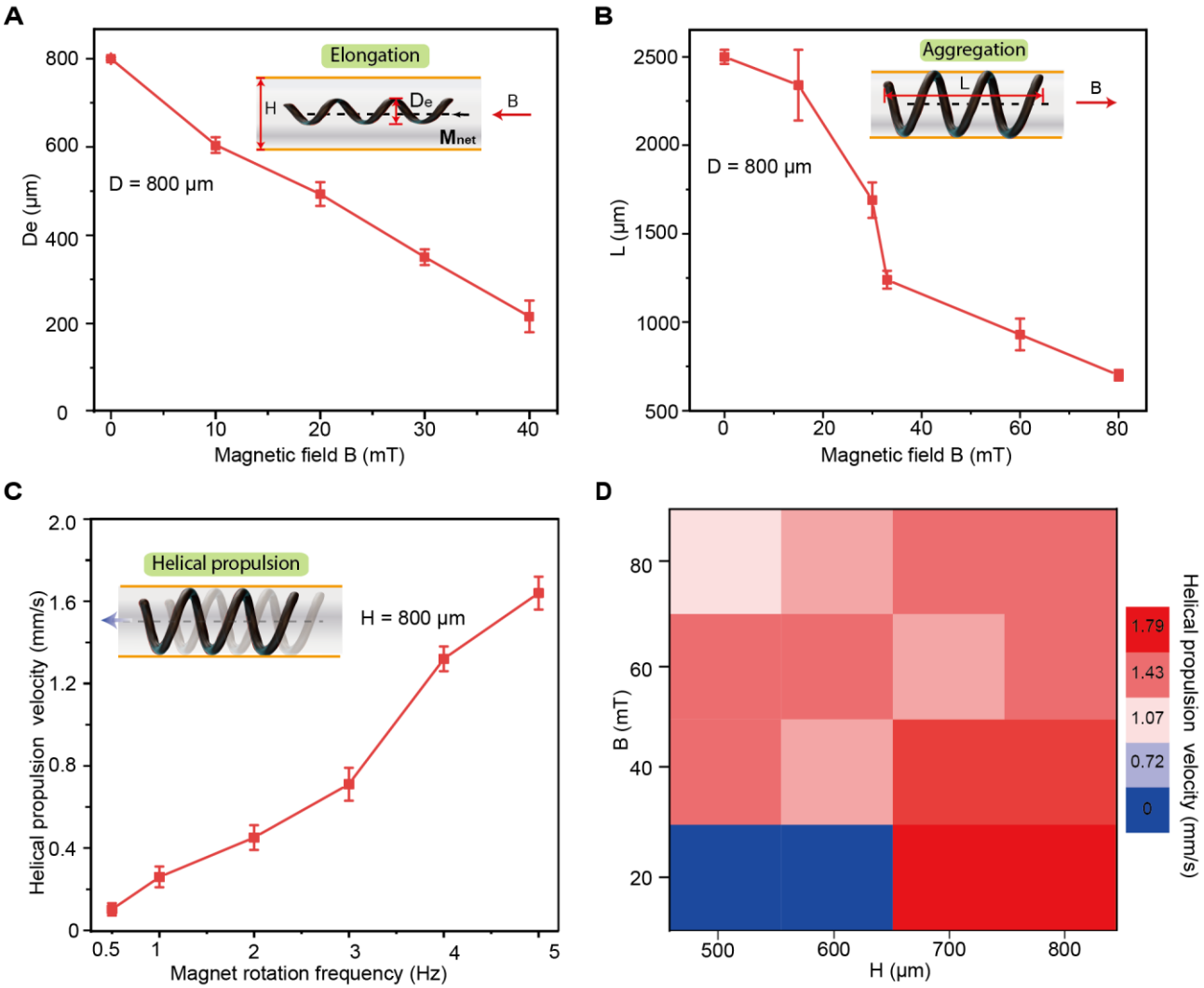

Fig. S3. Characterization of micro-fiberbots with helical diameter of 800μm under varying magnetic parameters. A, Helical diameter of micro-fiberbot as a function of actuation magnetic field strength. **B,** Length of the micro-fiberbot as a function of actuation magnetic field strength. **C,** Helical propulsion velocity as a function of magnet rotation frequency in the absence of flow (B = 40 mT). **D,** Helical propulsion velocity within vessels with different diameters H.

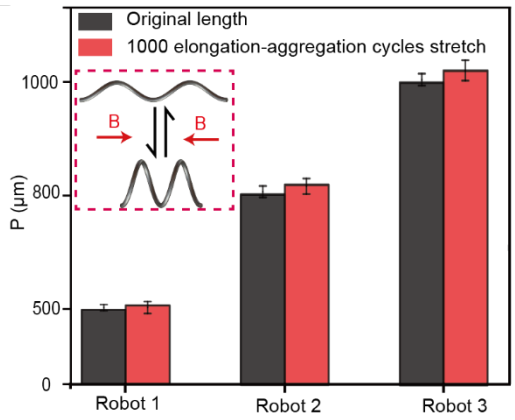

Fig. S4. Reversibility test of the shape morphing of the micro-fiberbot. After 1000 elongation-contraction cycles, the pitch of the four magnetic soft micro-fiberbots (Pitch p = 500, 800, and 1000 μm) remains almost unchanged.

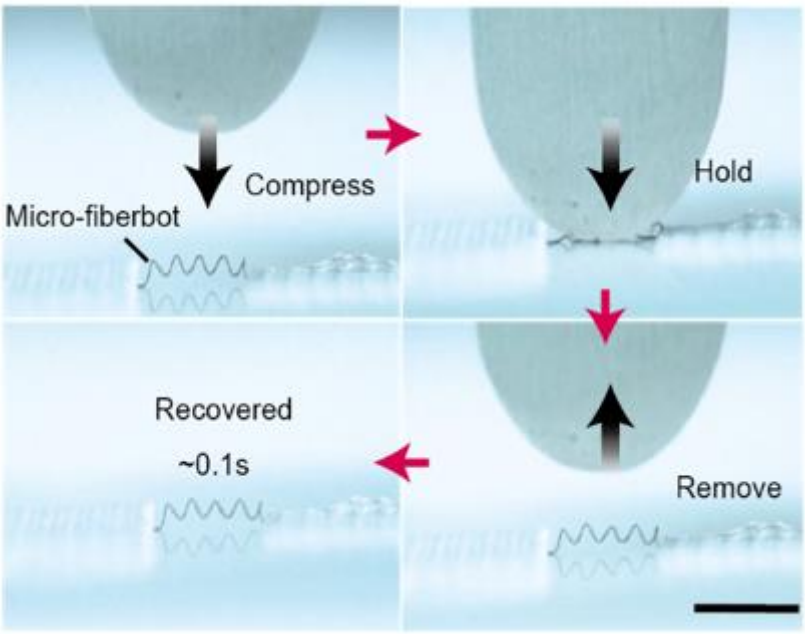

Fig. S5. High elasticity and mechanical robustness of the micro-fiberbot. The magnetic soft micro-fiberbot quickly (0.1 s) recovers to the initial helical shape after being compressed by a rigid punch. Scale bar, 5 mm.

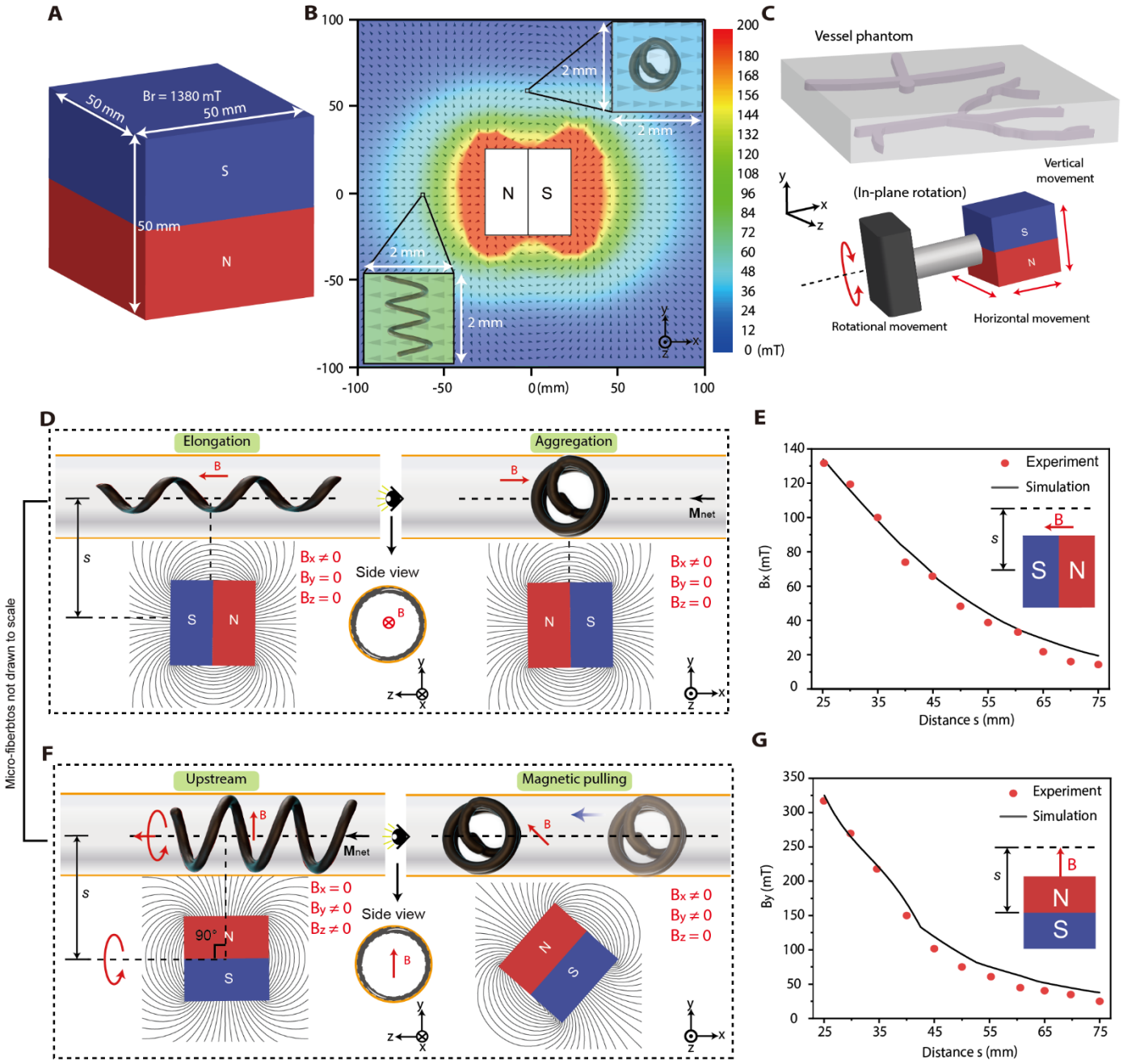

Fig. S6. Control strategy of micro-fiberbot using a cubic magnet. A, schematic of the cube magnet with a residual magnetic flux density Br =1380 mT. **B,** the magnetic fields around the cub magnet. **C,** the magnetic actuation for micro-fiber is achieved by dynamically controlling the vertical, horizontal, and rotational movements of the cube magnet. **D,** The magnetic soft micro-fiberbots can have aggregation and elongation shape-morphing by changing the external magnetic field. The elongated state of the micro-fiberbot is achieved by controlling the magnet to generate the magnetic field along with $\mathbf{M}_{net}$, and the aggregated state is achieved by controlling the magnet to generate the magnetic field opposite with $\mathbf{M}_{net}$. **E,** The magnetic field strength B_x as a function of distance *s* along the centerline of the magnet. **F,** the upstream helical propulsion is achieved by rotating the magnet in a clockwise manner, and magnetic pulling is achieved by moving the magnet. **G,** The magnetic field strength B_y as a function of distance *s* along the centerline of the magnetic.

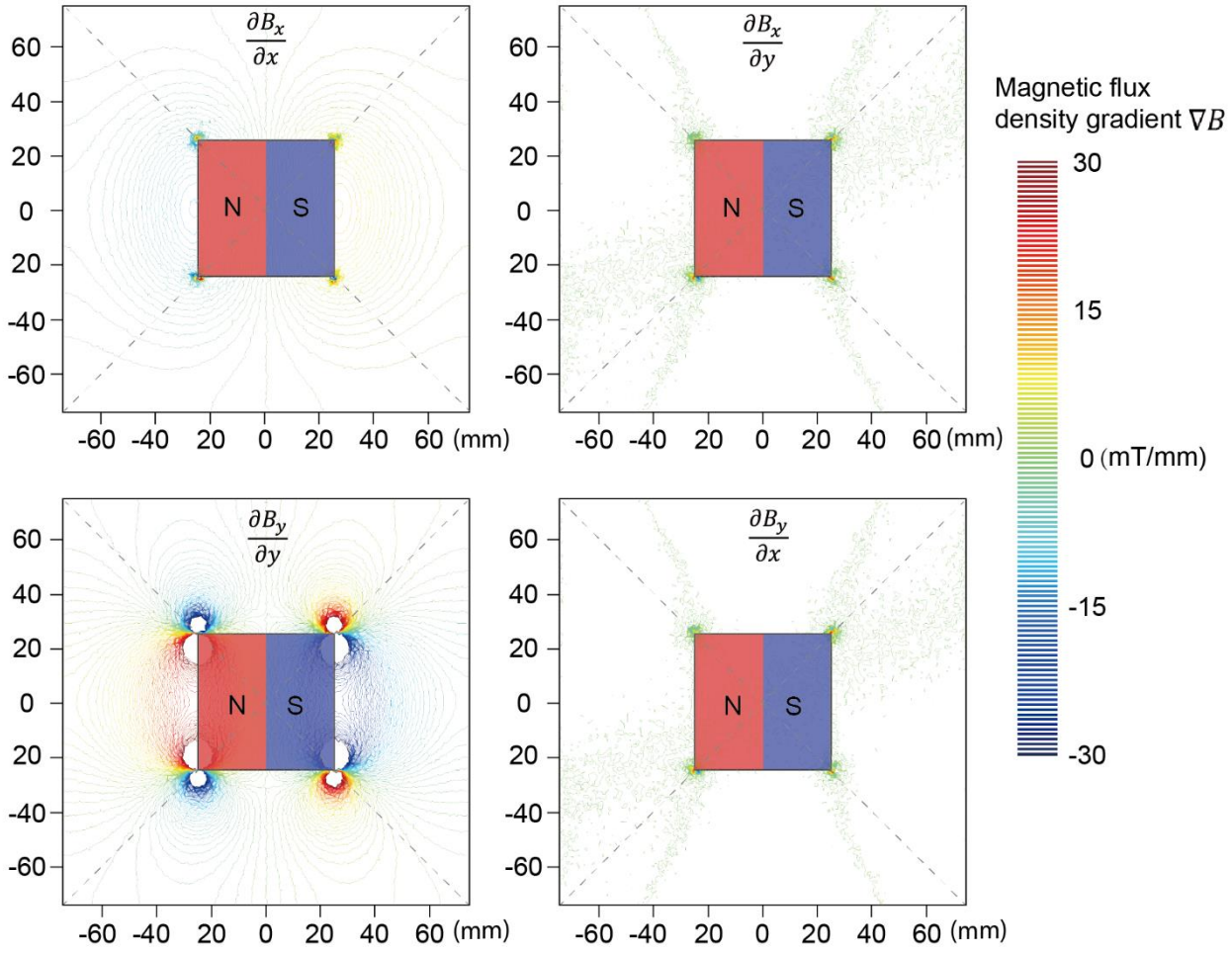

Fig. S7. Spatial magnetic gradient distribution of a cubic magnet with width of 50 mm.

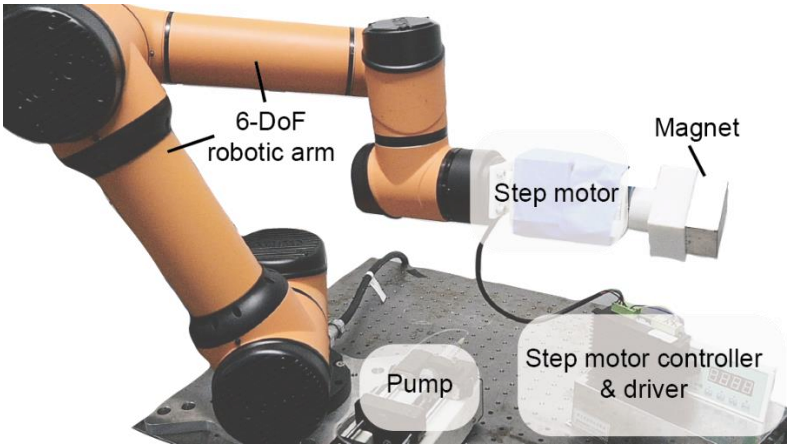

Fig. S8. Magnetic maneuvering system. The magnetic maneuvering system is composed of 6-DoF robotic arm, a step motor controller and driver, and a cubic magnet.

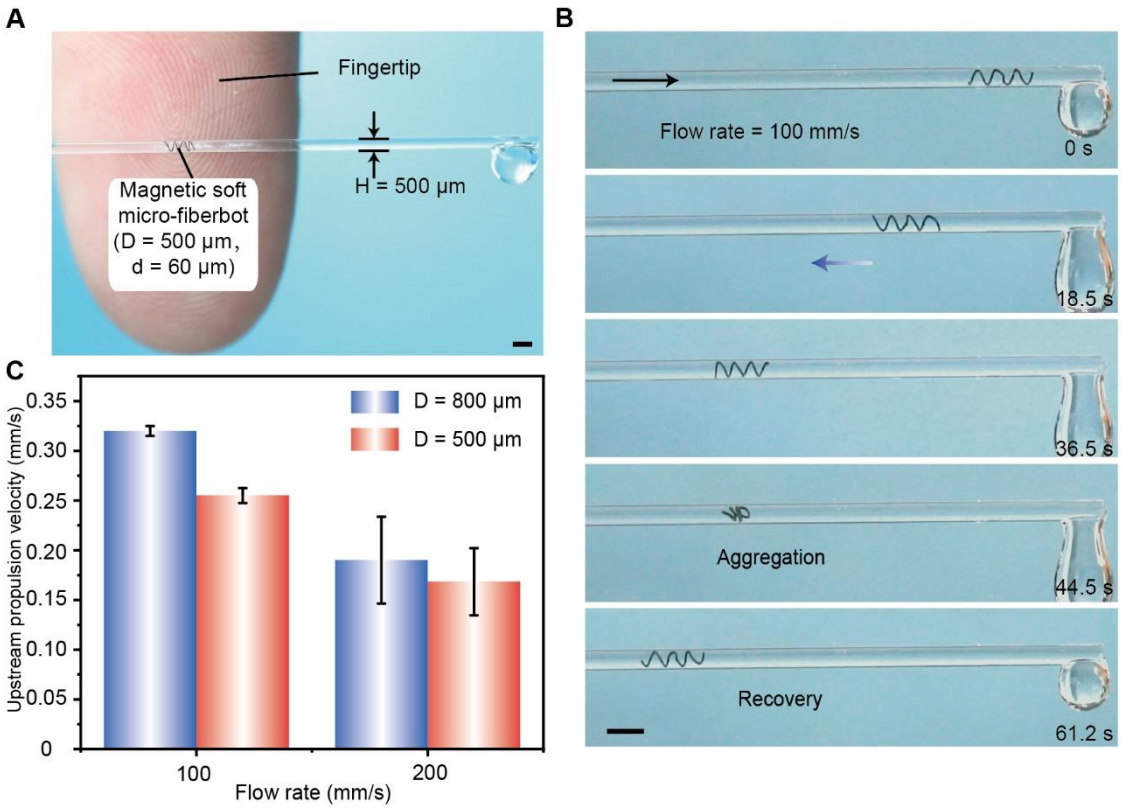

Fig. S9. Demonstration of shape-morphing capability and in-flow maneuverability of micro-fiberbot with 500 μm diameter. A, Image of a micro-fiberbot inside a tube with a 500μm diameter. **B,** The 500 μm micro-fiberbot can still have shape-morphing and upstream propulsion in a flow condition with 100mm/s flow rate. **C,** The upstream propulsion velocity of the 500 μm robot is comparable to that of the 800μm micro-fiberbot in both 100 mm/s and 200 mm/s flow. Scale bar, 1mm.

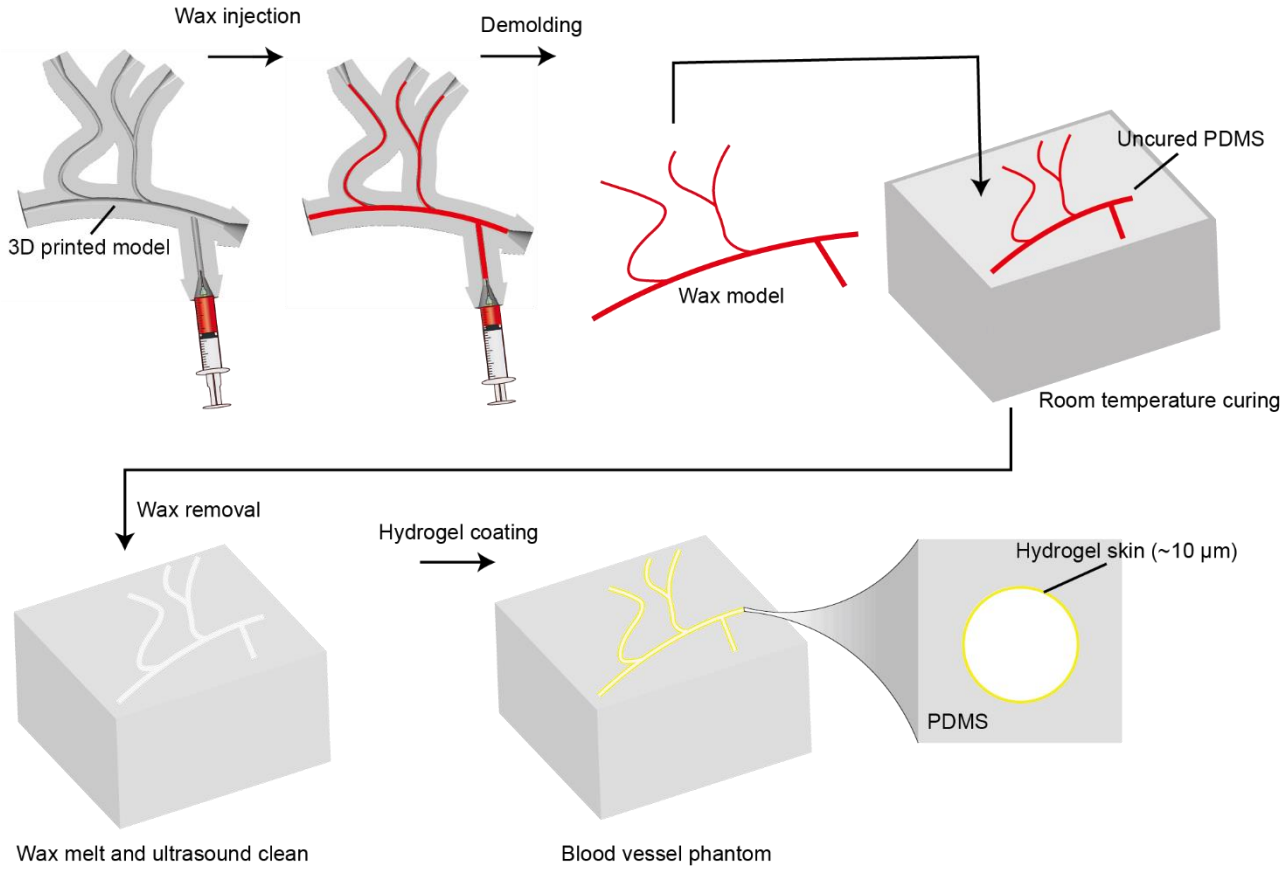

Fig. S10. Fabrication of blood vessel phantoms. The sacrificial template method was used to fabricate the vessel phantom. Melted wax was first injected into 3D-printed negative molds, and then solidified wax mold with the desired shape was carefully taken out. Next, the wax mold was immersed into uncured PDMS (mass ratio 10:1) and cured at room temperature (23℃) for 72 hours. Lastly, the phantoms were placed on a hot plate (120℃) to melt the wax and the vessel phantom with hollow lumen structure was placed in ultrasound cleaner with ethanol for 2 h. To obtain similar friction conditions to realistic blood vessels, a thin hydrogel layer (~ 10 μm) was coated in the inner surface of the hollow lumen structure *(12)*. Therefore, the vessel phantoms have similar young's modulus properties (2 MPa) and friction properties with the coefficient of 0.1.

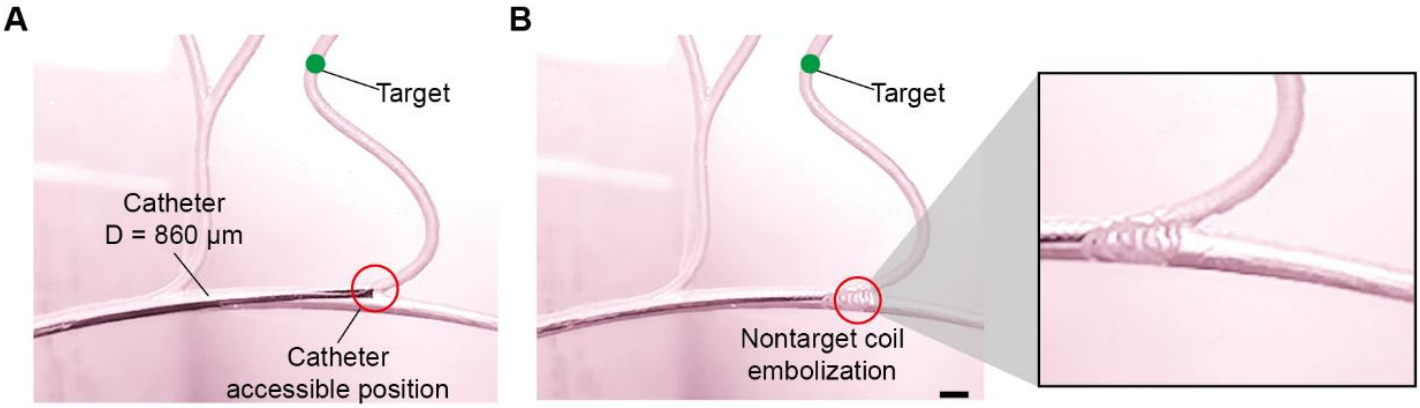

Fig. S11. Demonstration of nontarget coil embolization using commercial catheter. A, Commercial catheter can only reach the second bifurcation. B, The limited accessibility of catheter may lead nontarget coil embolization. Scale bar, 2mm.

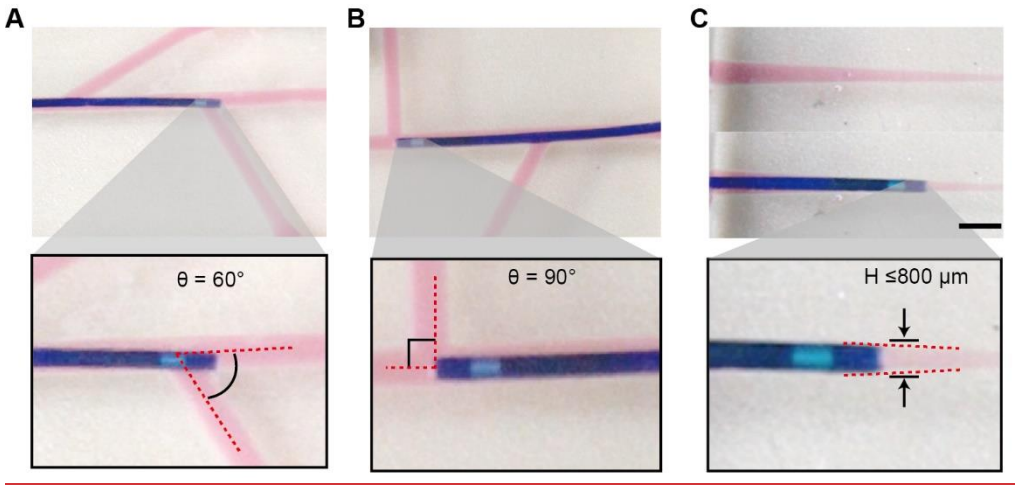

Fig. S12. Demonstration of the low steerability of commercial catheter. A-B, Commercial catheter cannot be steered to the bifurcation vascular phantom with bifurcation angle (A) θ = 60° and (B) 90°. **C**, Commercial catheter cannot access narrowing branches with diameter smaller than its tip. Scale bar, 2mm.

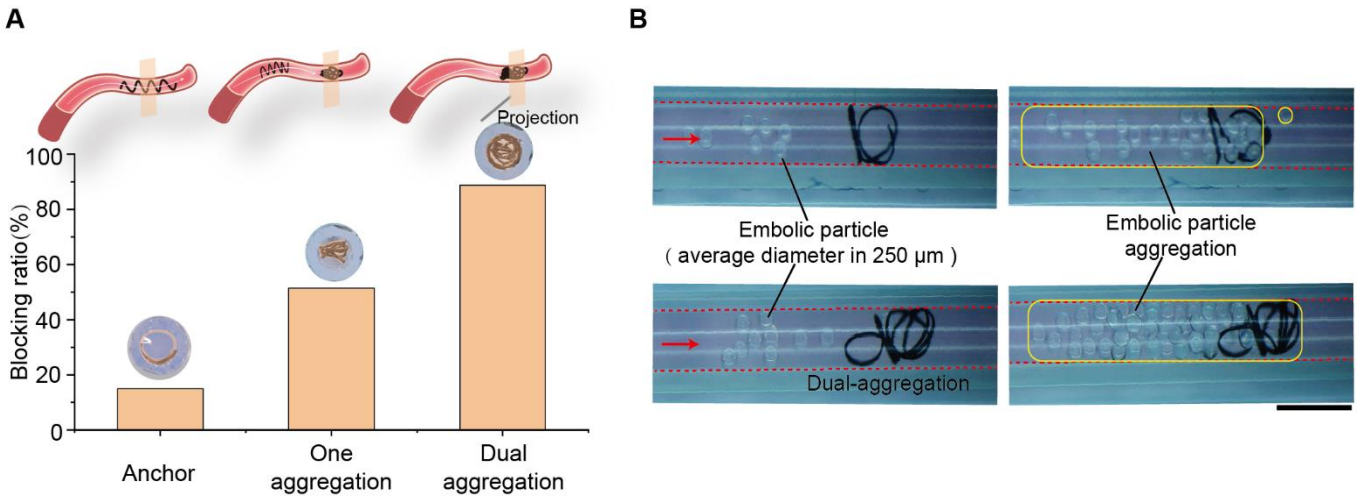

Fig. S13. Comparison of the blocking ratio between one micro-fiberbot aggregation and dual aggregation by two micro-fiberbots. A, the blocking ratio was calculated by cross-section area ratio between the aggregated micro-fiberbots and the blood vessels. B, Demonstration showing that particles are fully blocked with dual aggregated micro-fiberbots. Scale bar, 1 mm.

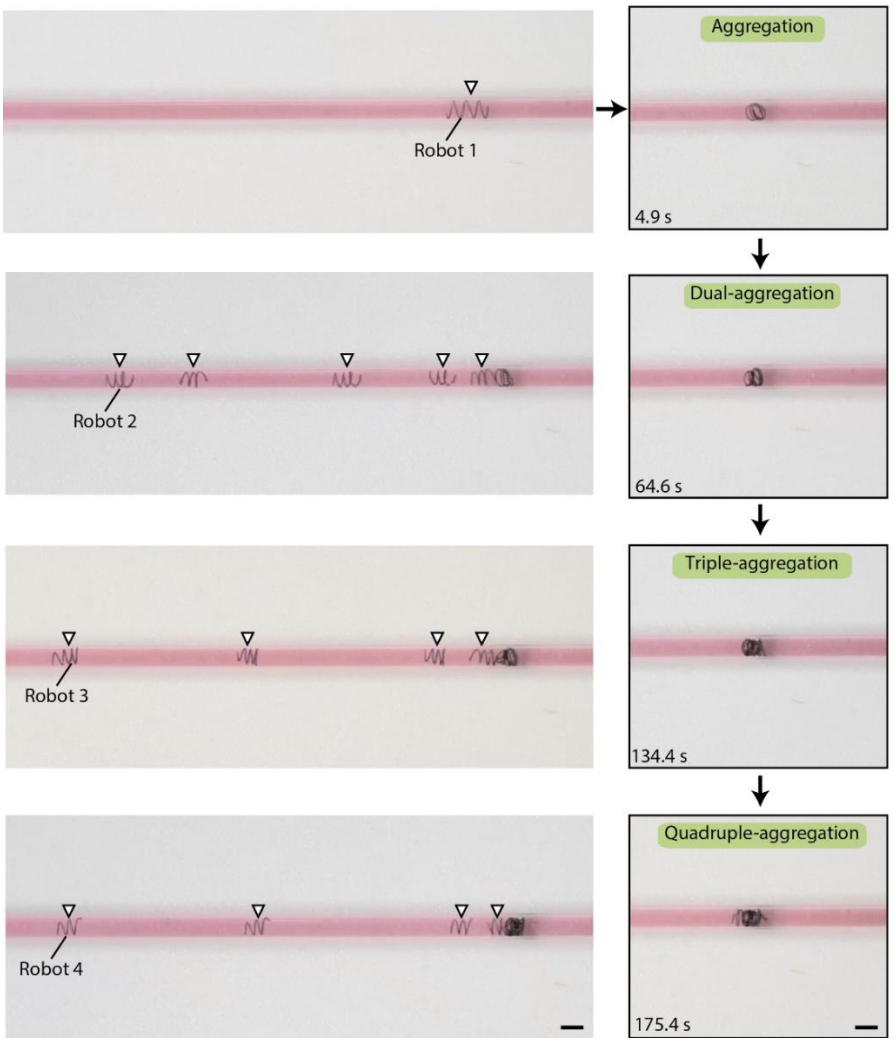

Fig. S14. Demonstration of four micro-fiberbot achieve quadruple-aggregation at the same target site in a vessel phantom. Scale bar, 1 mm.

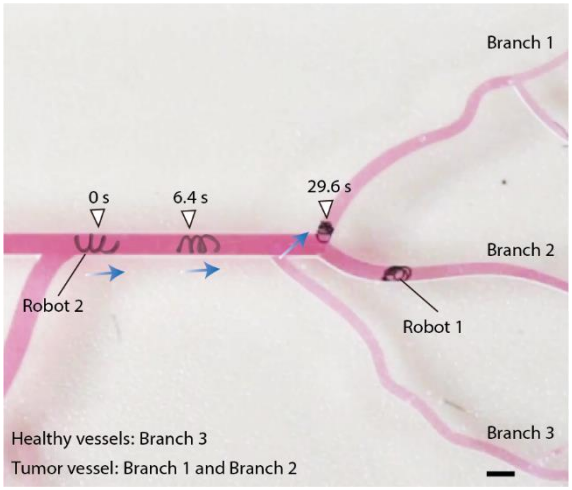

Fig. S15. Demonstration of micro-fiberbots achieve aggregation in different vessel branches. Scale bar, 1 mm.

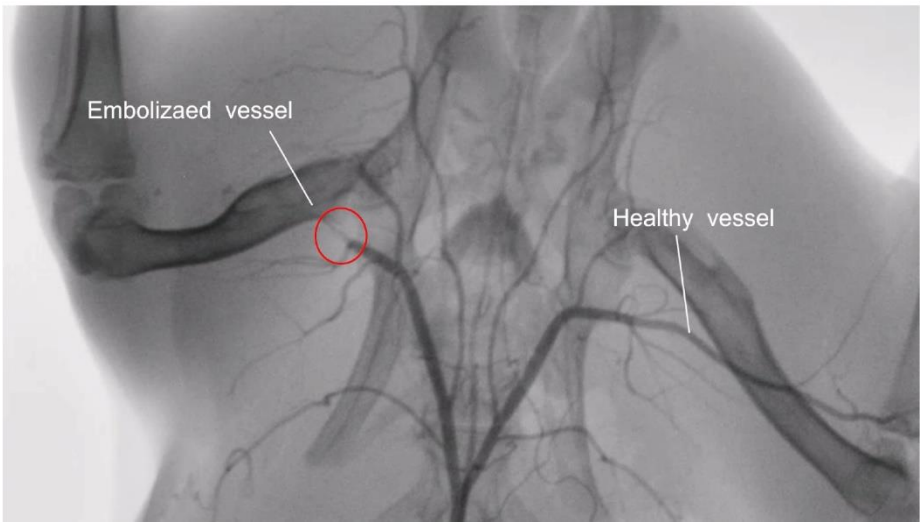

Fig. S16. Angiography of the rabbit blood vessels after 21 days embolization.

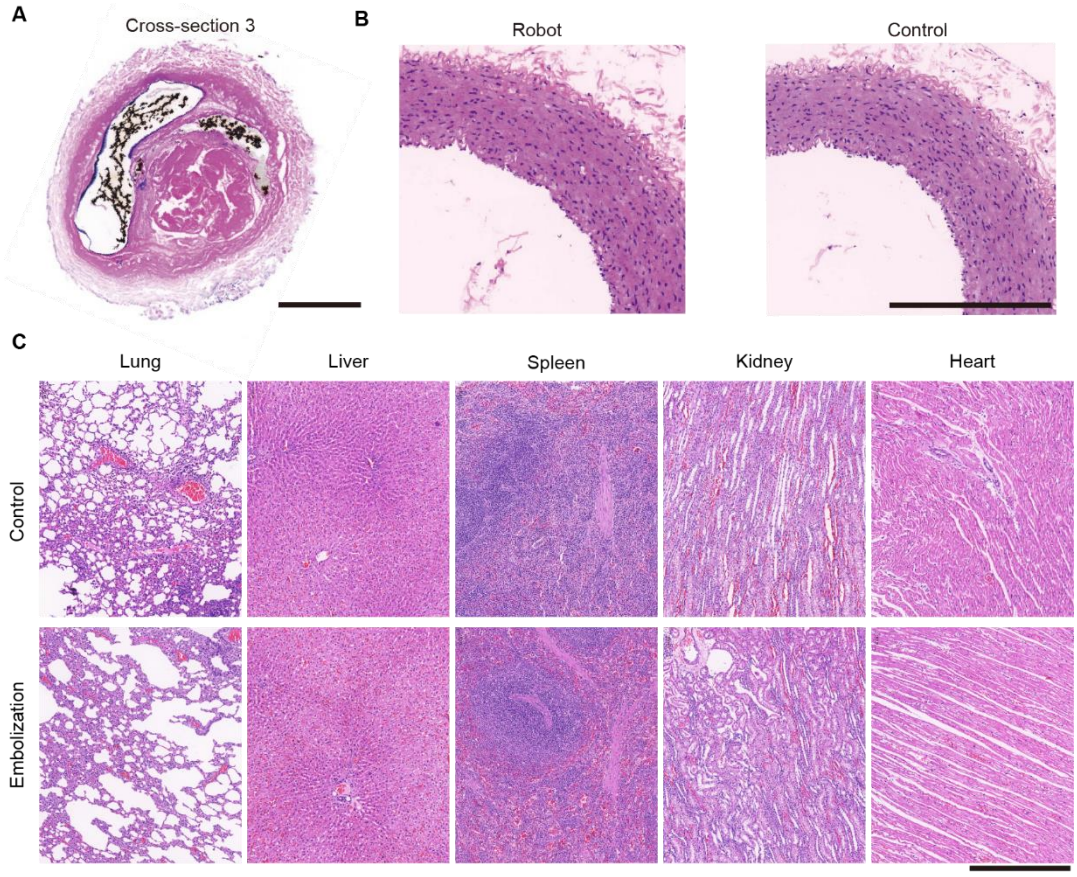

Fig. S17. Histology analysis of main organs of rabbits after two-week embolization surgery. A, The cross-section 3 of H&E staining cross-section images were selected from the proximal to distal blood vessels to validate the embolization results. Scale bar, 250 μm. **B,** The H&E staining cross-section image of the rabbit femoral artery. The sample for the soft micro-fiberbot group was collected after locomotion. Scale bar, 250 μm. **C,** no inflammation or pathological abnormalities were observed in the samples collected from the control group and embolization group of rabbits. Scale bar, 500 μm.

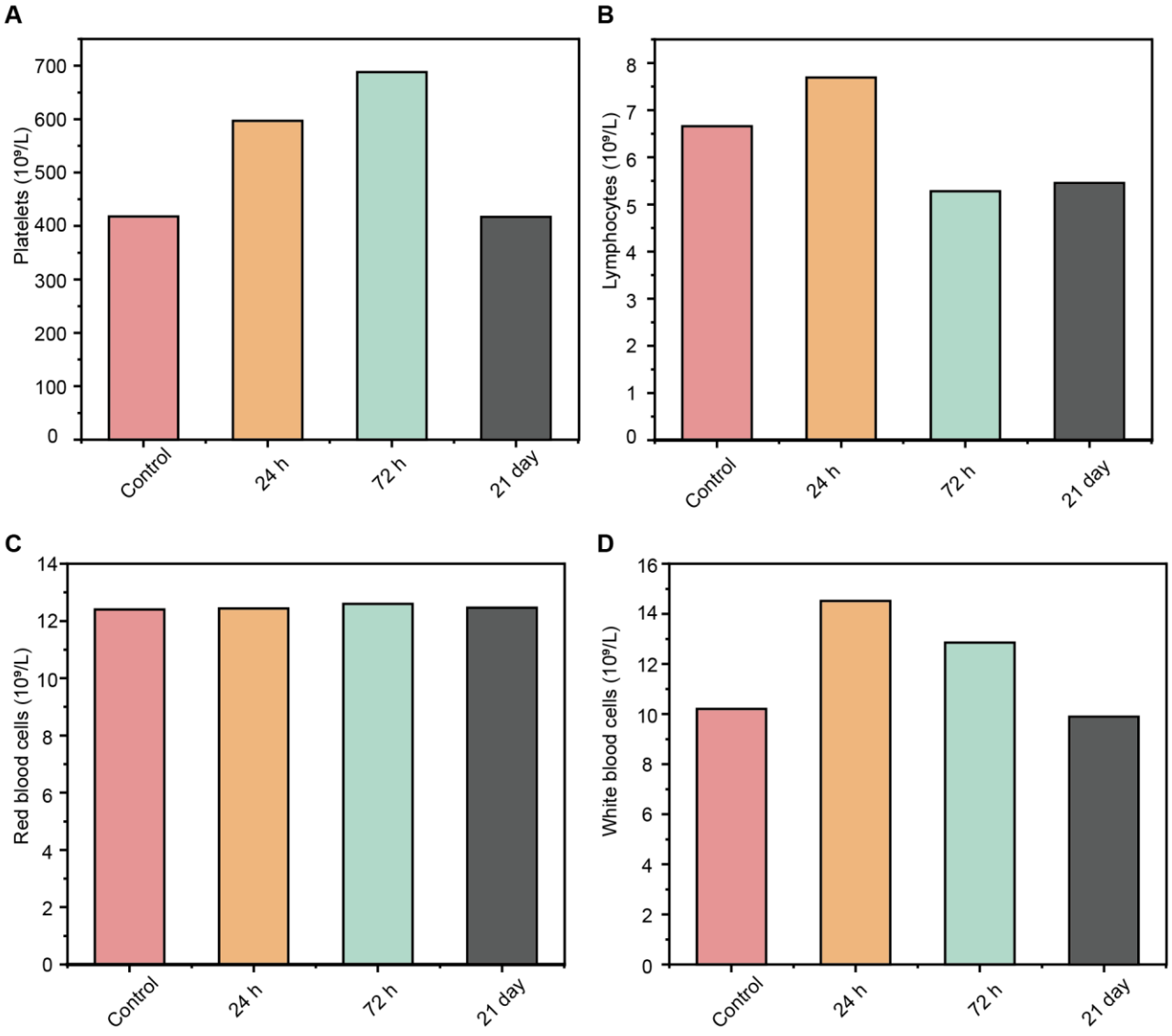

Fig. S18. Comprehensive blood cell counts taken from rabbit before and after embolization (24h, 72h, 21 day).

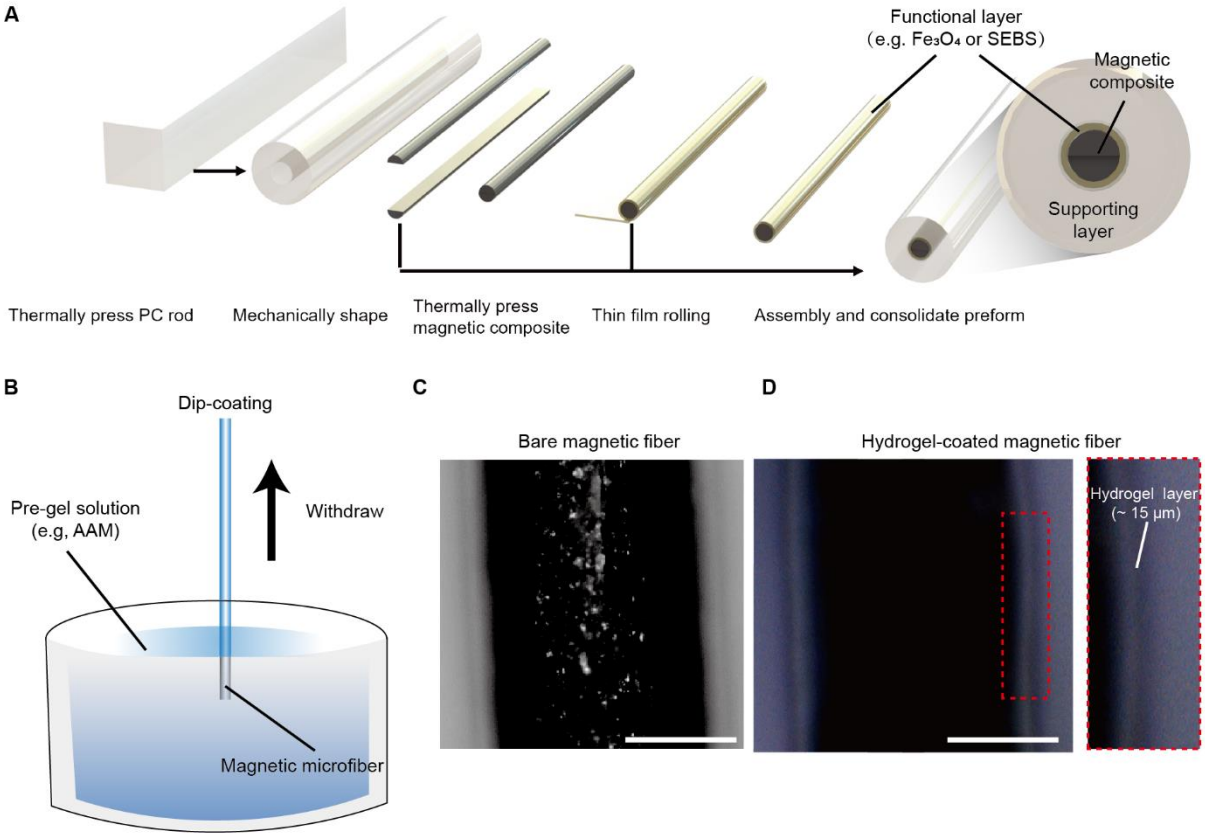

Fig. S19. Fabrication of coating hydrogel skin. A Schematic of the steps used to fabricate millimeter-scale magnetic composite preform with embedded functional layers. **B,** Schematic of dip-coating hydrogel on a magnetic fiber in pre-gel solution (AAM). **C,** The optical imaging of bare magnetic fiber shows that the magnetic particles are exposed without hydrogel coating. **D,** After hydrogel coating, the magnetic particles were isolated and a hydrogel layer (~15 μm) was observed. Scale bar 50 μm.

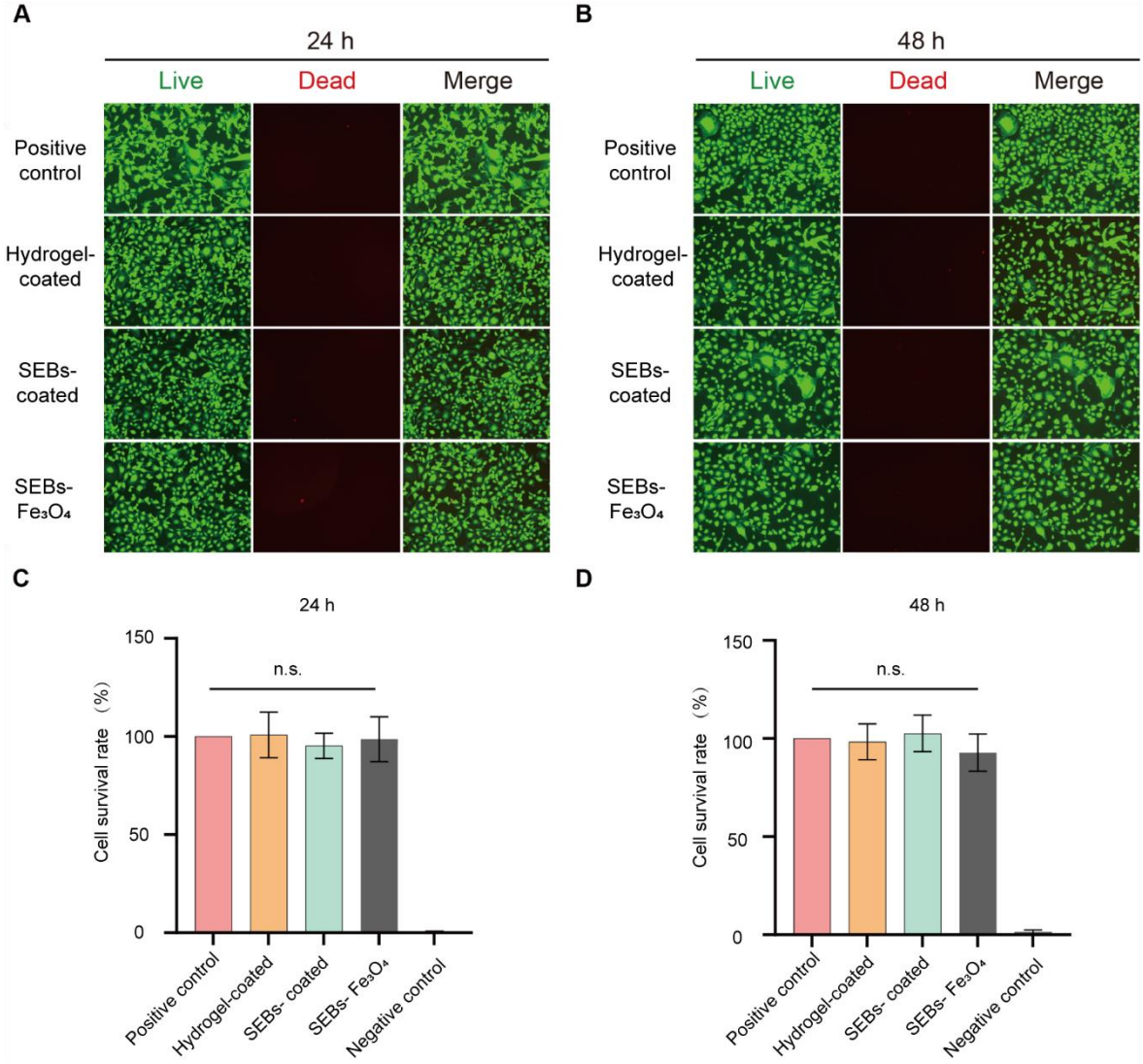

Fig. S20. Cell viability tests of magnetic composites with different coatings. A, Fluorescence microscopic images of human cardiac microvascular endothelial cells incubated with the composites at the exposure times of 24 hours and 48 hours, respectively. **B** Relative cell survival rate of positive control, hydrogel-coated, SEBs-coated, SEBs-Fe_3O_4 magnetic soft micro-fiberbots.

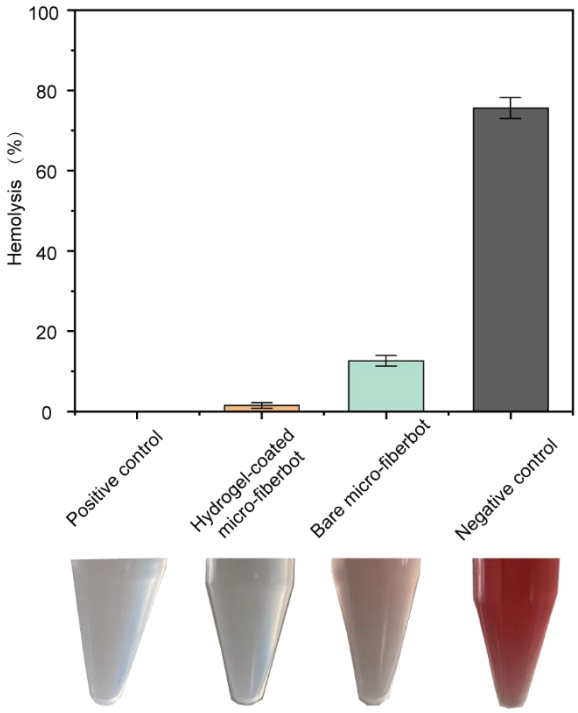

Fig. S21. Analysis of blood cell hemolysis of positive control, negative control, bare micro-fiberbots and hydrogel-coated micro-fiberbots.

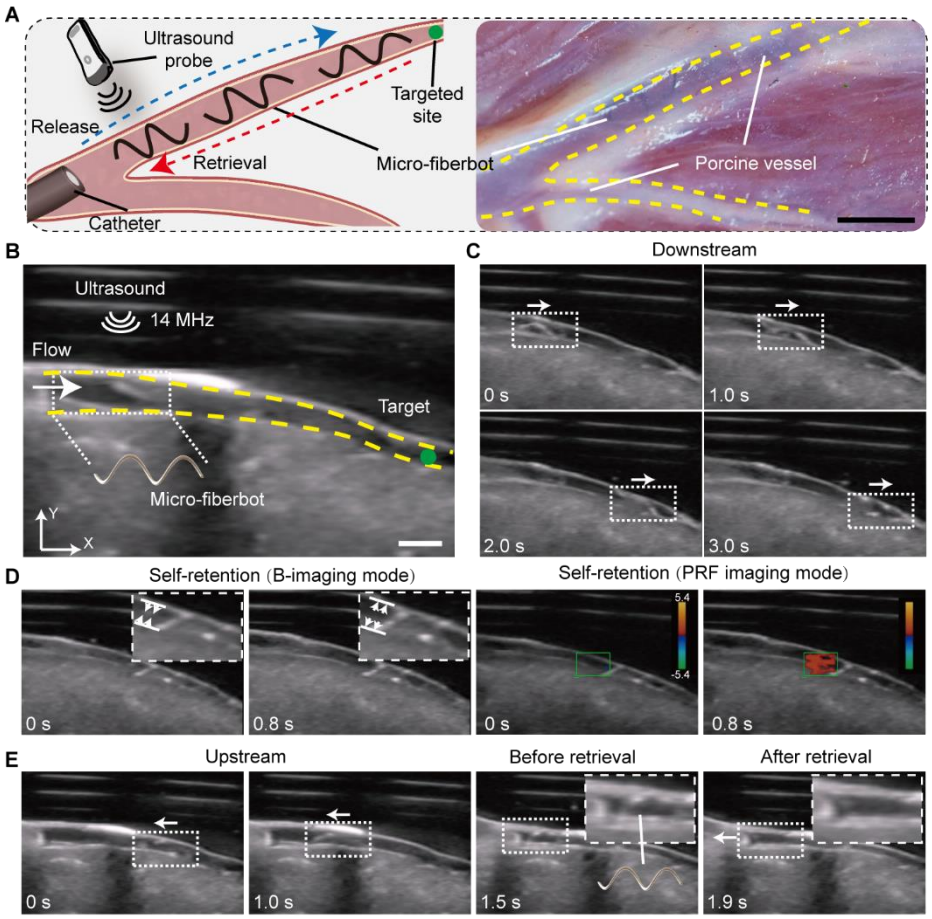

Fig. S22. Ex vivo demonstration of real-time ultrasound tracking capability of micro-fiberbot. A, Schematic of magnetic soft micro-fiberbots locomotion and retrieval for targeted drug delivery under real-time ultrasound imaging. Right: The optical images of magnetic soft micro-fiberbots navigating in a porcine coronary artery. Scale bar, 5 mm. **B,** Real-time ultrasound imaging-tracked navigation of magnetic soft micro-fiberbots controlled by the external magnetic manipulation system in an ex vivo porcine coronary artery under the flow. The white arrow indicates the flow directions. **C,** Downstream navigation of magnetic soft micro-fiberbots to a targeted site. Red arrows show the navigation directions. **D,** Magnetic soft micro-fiberbots self-retained in flow environments with dynamically changed porcine coronary artery diameters, the insets show the enlarged images of the magnetic soft micro-fiberbots. PRF: 1.0 kHz. **E,** Upstream navigation and catheter retrieval of magnetic soft micro-fiberbots. Scale bar, 2 mm (D to E).

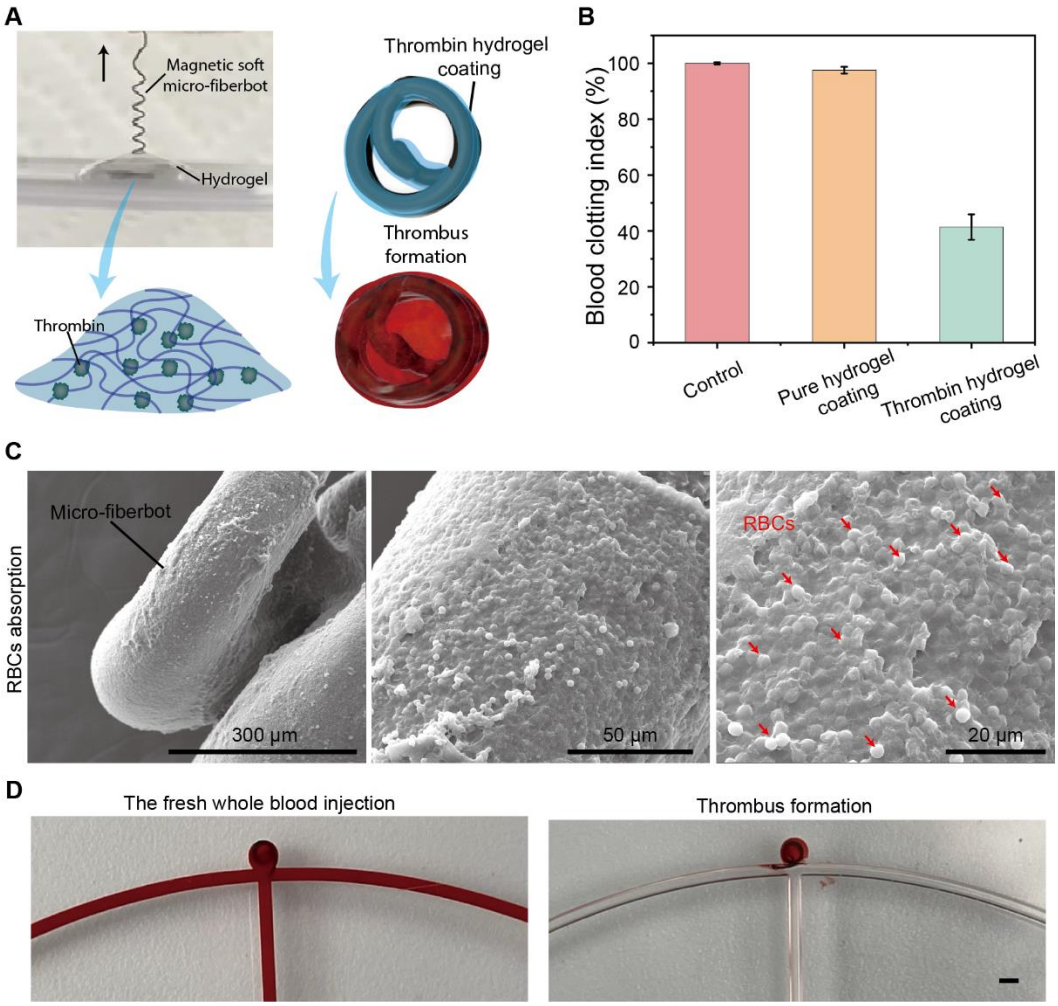

Fig. S23. Thrombin-hydrogel coating of the micro-fiberbot promotes thrombus formation. A, Experimental image demonstrating the dip coating method used to form a thin layer of thrombin-hydrogel on the micro-fiberbot. Scale bar, 1 mm. **B,** Blood clotting index of control, pure hydrogel coating, and thrombin-hydrogel coating groups. **C,** Scanning electron microscope (SEM) image displaying red blood cell (RBC) absorption on the micro-fiberbot. **D,** Injection of blood to stimulate thrombus formation within the aneurysm phantom. Scale bar, 1mm.

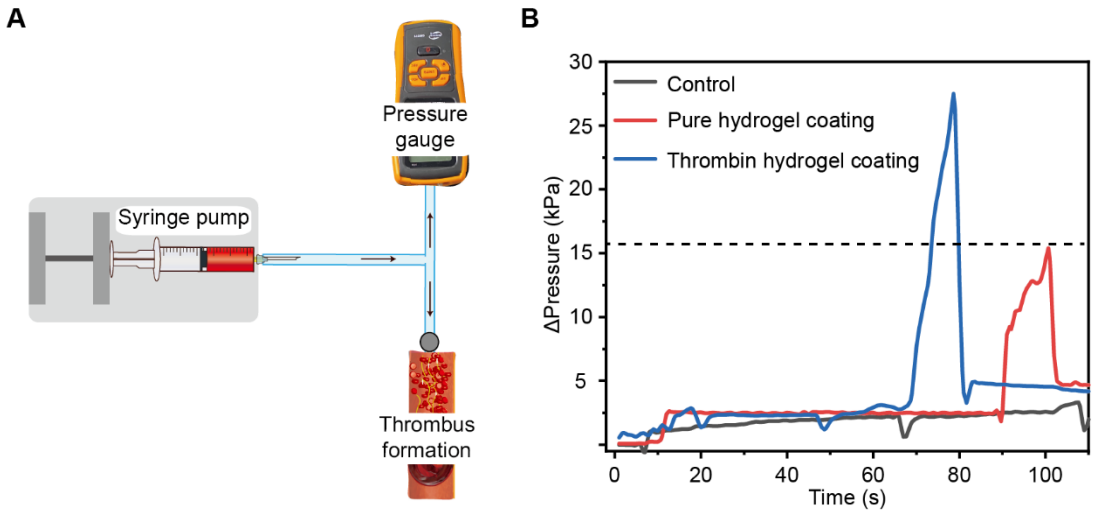

Fig. S24. Pressure assessment of the micro-fiberbot within a vessel phantom. A, Schematic of the in vitro occlusion setup employing a syringe pump and a pressure gauge to measure the pressure needed to drive blood through the tube. **B,** Pressure as a function of time for control (blood alone), pure hydrogel coating, and thrombin hydrogel coating.

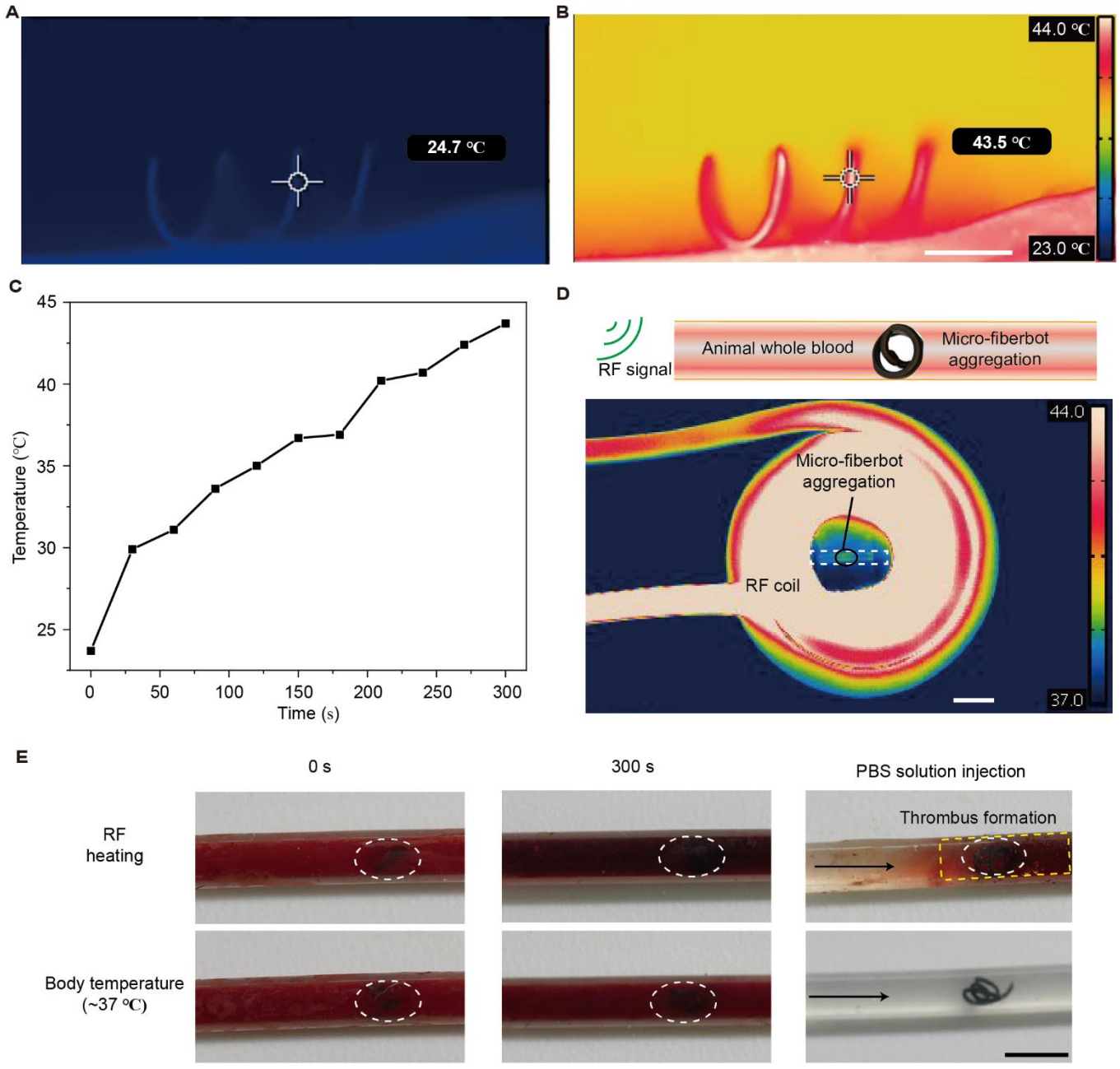

Fig. S25. Demonstration of micro-fiberbot under RF signal for local hyperthermia and thrombus formation. A, Infrared picture shows the temperature of micro-fiberbots before RF heating. **B**, Infrared picture shows the temperature of micro-fiberbots after RF heating. **C,** The temperature change of micro-fiberbot in 300 seconds. **D,** Micro-fiberbot was placed on the vessel phantom with animal whole blood and then heated by RF coil. **E,** After 5 min RF heating, the thrombus formation was observed. As a comparison, without RF heating, no significant thrombus formation.

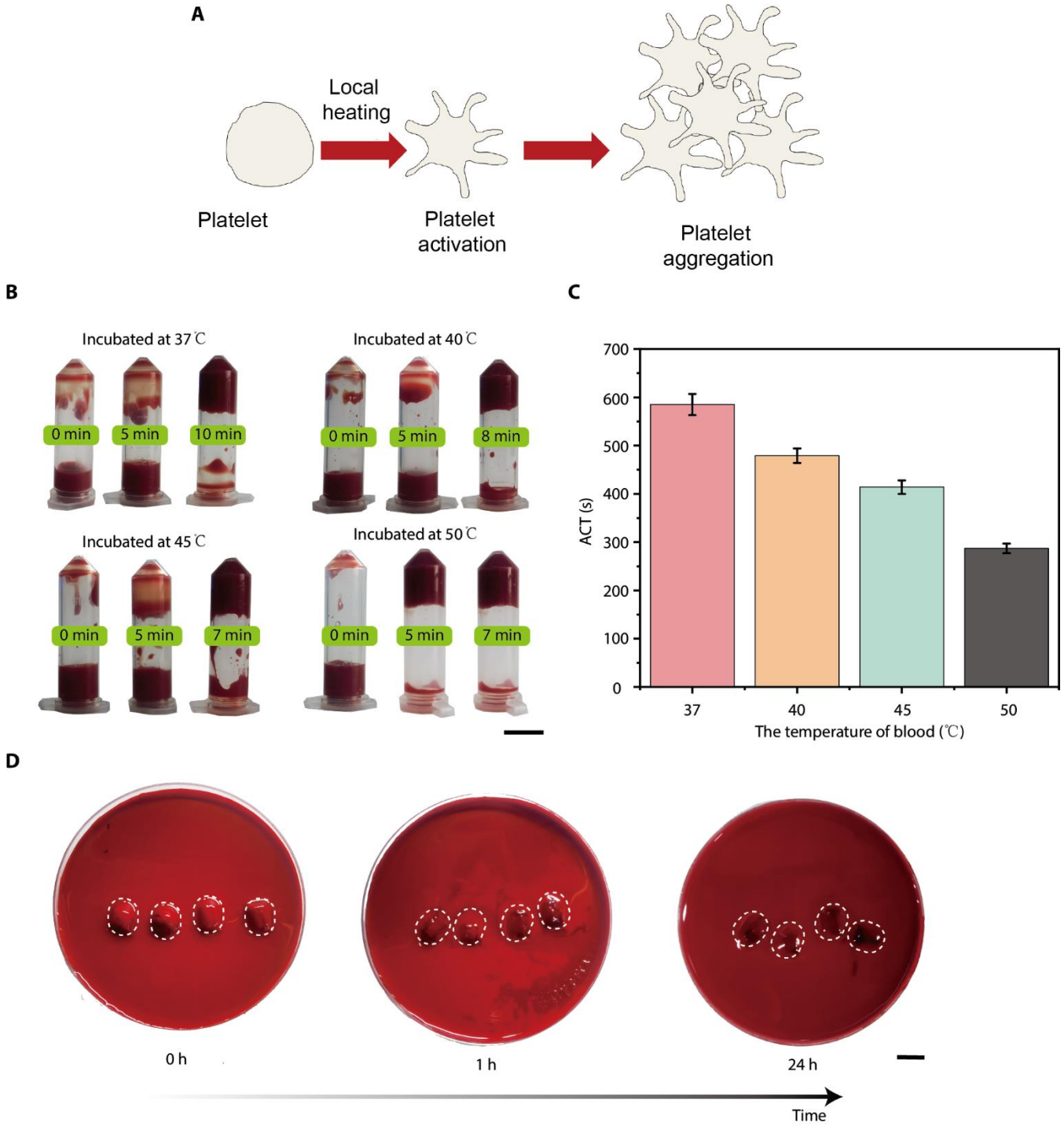

Fig. S26. Thrombus formation when incubated in different temperatures. A, Schematic illustration of platelet activation and aggregation. B, Images show the porcine whole blood incubated in four feature Temperature with different times. C, Activated coagulation time (ACT) at different incubated temperatures. D, Temporal shape variation of formed thrombus in anticoagulated porcine blood. Scale bar, 10 mm.

References

1. Y. Alapan, U. Bozuyuk, P. Erkoc, A. C. Karacakol, M. Sitti, Multifunctional surface microrollers for targeted cargo delivery in physiological blood flow. *Sci. Robot.* **5**, eaba5726 (2020).
2. Q. Wang, K. F. Chan, K. Schweizer, X. Du, D. Jin, S. C. H. Yu, B. J. Nelson, L. Zhang, Ultrasound Doppler-guided real-time navigation of a magnetic microswarm for active endovascular delivery. *Sci. Adv.* **7**, eabe5914 (2021).
3. Q. Wang, X. Du, D. Jin, L. Zhang, Real-Time Ultrasound Doppler Tracking and Autonomous Navigation of a Miniature Helical Robot for Accelerating Thrombolysis in Dynamic Blood Flow. *Acs Nano*, **16**, 604-616 (2022).
4. F. E. Stokes, R. A. King, Flow-induced vibration of helical coil compression springs, in SMiRT 7, 22-26 August 1983, Chicago, IL, pp. 305-312.
5. T. Gopesh, J. H. Wen, D. Santiago-Dieppa, B. Yan, J. S. Pannell, A. Khalessi, A. Norbash, J. Friend, Soft robotic steerable microcatheter for the endovascular treatment of cerebral disorders. *Sci. Robot.* **6**, eabf0601 (2021).
6. M. F. Phelan, M. E. Tiryaki, J. Lazovic, H. Gilbert, M. Sitti, Heat-mitigated design and Lorentz force-based steering of an MRI-driven microcatheter toward minimally invasive surgery. *Adv. Sci.* **9**, 2105352 (2022).
7. Y. Kim, E. Genevriere, P. Harker, J. Choe, M. Balicki, R. W. Regenhardt, J. E. Dmytriw, A. B. Patel, X. Zhao, Telerobotic neurovascular interventions with magnetic manipulation. *Sci. Robot.* **7**, eabg9907 (2022).
8. L. Pancaldi, P. Dirix, A. Fanelli, A. M. Lima, N. Stergiopulos, P. J. Mosimann, D. Ghezzi, M. S. Sakar, Flow driven robotic navigation of microengineered endovascular probes. *Nat. Commun.* **11**, 6356 (2020).
9. J. Law, X. Wang, M. Luo, L. Xin, X. Du, W. Dou, T. Wang, G. Shan, Y. Wang, P. Song, X. Huang, J. Yu, Y. Sun, Microrobotic swarms for selective embolization. *Sci. Adv.* **8**, eabm5752 (2022).
10. N. Li, F. Michaud, Z. Nosrati, D. Loghin, C. Tremblay, R. Plantefève, K. Saatchi, U. O. Häfeli, S. Martel, G. Soulez, MRI-compatible injection system for magnetic microparticle embolization. *IEEE Trans. Biomed. Eng.* **66**, 2331-2340 (2018).
11. Z. Li, Z. Chen, Y. Gao, Y. Xing, Y. Zhou, Y. Luo, W. Xu, Z. Chen, X. Gao, K. Gupta, K. Anbalakan, L. Chen, C. Liu, J. Kong, H. L. Leo, C. Hu, H. Yu, Q. Guo, Shape memory micro-anchors with magnetic guidance for precision micro-vascular deployment. *Biomaterials* **283**, 121426 (2022).
12. G. Parada, Y. Yu, W. Riley, S. Lojovich, D. Tshikudi, Q. Ling, Y. Zhang, J. Wang, L. Ling, Y. Yang, S. Nadkarni, C. Nabzdyk, X. Zhao, Ultrathin and robust hydrogel coatings on cardiovascular medical devices to mitigate thromboembolic and infectious complications. *Adv. Healthc. Mater.* **9**, 2001116 (2020).

Legends for Movies S1 to S14

Movie S1. Overview movie of magnetic soft micro-fiberbots for robotic embolization.
Movie S2. Shape morphing capability of micro-fiberbots under magnetic fields.
Movie S3. Magnetic maneuvering of micro-fiberbot in flow condition.
Movie S4 Demonstration of shape-morphing capability and in-flow maneuverability of micro-fiberbot with 500 μm diameter.
Movie S5. Catheter-assisted deployment of micro-fiberbots.
Movie S6. Demonstration of micro-fiberbots steering in bifurcation branches of blood vessel phantom.
Movie S7. Demonstration of micro-fiberbots steering in a narrowing blood vessel phantom.
Movie S8. Demonstration of micro-fiberbots steering in an S-shaped blood vessel phantom.
Movie S9. Demonstration of micro-fiberbots steering in a 3D blood vessel phantom.
Movie S10. In vitro demonstration of aneurysm embolization
Movie S11. In vitro demonstration of tumor coil embolization.
Movie S12. Dual-aggregation of micro-fiberbots
Movie S13. In vitro demonstration of particle embolization protection and retrieval.
Movie S14. In vivo demonstration of robotic embolization in a rabbit.